The Astrophysical Journal Letters, 919:L24 (17pp), 2021 October 1 https://doi.org/10.3847/2041-8213/ac223b

A Local Universe Host for the Repeating Fast Radio Burst FRB 20181030A

M. Bhardwaj[1,2], A. Yu. Kirichenko[3,4], D. Michilli[1,2], Y. D. Mayya[5], V. M. Kaspi[1,2], B. M. Gaensler[6,7], M. Rahman[8], S. P. Tendulkar[9,10], E. Fonseca[1,2], Alexander Josephy[1,2], C. Leung[11,12], Marcus Merryfield[1,2], Emily Petroff[1,2,13,18], Z. Pleunis[1,2], Pranav Sanghavi[14,15], P. Scholz[6], K. Shin[11,12], Kendrick M. Smith[16], and I. H. Stairs[17]

[1] Department of Physics, McGill University, 3600 Rue University, Montréal, QC H3A 2T8, Canada; mohit.bhardwaj@mail.mcgill.ca
[2] McGill Space Institute, McGill University, 3550 Rue University, Montréal, QC H3A 2A7, Canada
[3] Instituto de Astronomía, Universidad Nacional Autónoma de México, Apdo. Postal 877, Ensenada, Baja California 22800, México
[4] Ioffe Institute, 26 Politekhnicheskaya St., St. Petersburg 194021, Russia
[5] Instituto Nacional de Astrofísica, Óptica y Electrónica, Luis Enrique Erro 1, Tonantzintla 72840, Puebla, Mexico
[6] Dunlap Institute for Astronomy & Astrophysics, University of Toronto, 50 St. George Street, Toronto, ON M5S 3H4, Canada
[7] David A. Dunlap Department of Astronomy & Astrophysics, University of Toronto, 50 St. George Street, Toronto, ON M5S 3H4, Canada
[8] Sidrat Research, P.O. Box 73527 RPO Wychwood, Toronto, Ontario, M6C 4A7, Canada
[9] Department of Astronomy and Astrophysics, Tata Institute of Fundamental Research, Mumbai, 400005, India
[10] National Centre for Radio Astrophysics, Post Bag 3, Ganeshkhind, Pune, 411007, India
[11] MIT Kavli Institute for Astrophysics and Space Research, Massachusetts Institute of Technology, 77 Massachusetts Avenue, Cambridge, MA 02139, USA
[12] Department of Physics, Massachusetts Institute of Technology, 77 Massachusetts Avenue, Cambridge, MA 02139, USA
[13] Anton Pannekoek Institute for Astronomy, University of Amsterdam, Science Park 904, 1098 XH Amsterdam, The Netherlands
[14] Lane Department of Computer Science and Electrical Engineering, 1220 Evansdale Drive, P.O. Box 6109, Morgantown, WV 26506, USA
[15] Center for Gravitational Waves and Cosmology, West Virginia University, Chestnut Ridge Research Building, Morgantown, WV 26505, USA
[16] Perimeter Institute for Theoretical Physics, 31 Caroline Street N, Waterloo, ON N25 2YL, Canada
[17] Dept. of Physics and Astronomy, 6224 Agricultural Road, Vancouver, BC V6T 1Z1 Canada
Received 2021 July 1; revised 2021 August 9; accepted 2021 August 27; published 2021 September 30

Abstract

We report on the host association of FRB 20181030A, a repeating fast radio burst (FRB) with a low dispersion measure (103.5 pc cm^{-3}) discovered by the CHIME/FRB Collaboration et al. Using baseband voltage data saved for its repeat bursts, we localize the FRB to a sky area of 5.3 $arcmin^2$ (90% confidence). Within the FRB localization region, we identify NGC 3252 as the most promising host with an estimated chance-coincidence probability $<2.5\times10^{-3}$. Moreover, we do not find any other galaxy with $M_r<-15$ AB mag within the localization region to the maximum estimated FRB redshift of 0.05. This rules out a dwarf host 5 times less luminous than any FRB host discovered to date. NGC 3252 is a star-forming spiral galaxy and at a distance of ≈20 Mpc, it is one of the closest FRB hosts discovered thus far. From our archival radio data search, we estimate a 3σ upper limit on the luminosity of a persistent compact radio source (source size <0.3 kpc at 20 Mpc) at 3 GHz to be 2×10^{26} erg s^{-1} Hz^{-1}, at least 1500 times smaller than that of the FRB 20121102A persistent radio source. We also argue that a population of young millisecond magnetars alone cannot explain the observed volumetric rate of repeating FRBs. Finally, FRB 20181030A is a promising source for constraining FRB emission models due to its proximity and we strongly encourage its multi-wavelength follow-up.

Unified Astronomy Thesaurus concepts: Radio transient sources (2008); Radio bursts (1339)

1. Introduction

Fast radio bursts (FRBs) are enigmatic radio pulses of high brightness temperature (~10^{35} K) and millisecond duration (Lorimer et al. 2007; Thornton et al. 2013). In spite of the fact that more than 500 FRBs have been discovered to date,[19] their nature continues to be a subject of intense debate, owing in part to a limited sample of localized FRBs. Furthermore, the FRBs exhibit a diverse range of phenomenology: most of the discovered sources are apparently non-repeating, but a small fraction are observed to repeat. Among the repeating FRBs, two thus far have shown evidence of periodic repetitions (CHIME/FRB Collaboration et al. 2020a; Cruces et al. 2020; Rajwade et al. 2020). As a result, a plethora of theories has been proposed to explain the FRB sources' disparate behavior (see Platts et al. 2019, for a catalog of proposed models).

To unveil the nature of FRB sources, detailed studies of FRB hosts and their local environments are a promising way forward (Nicholl et al. 2017; Li & Zhang 2020). Currently, only 15 published FRBs have been sufficiently well localized on the sky to allow their host galaxies to be identified.[20] All localized FRBs except FRB 20200120E in M81 (Bhardwaj et al. 2021) are located at redshifts ranging from 0.03 to 0.66 where the detailed study of the FRB local environment is limited by the sensitivity of current telescopes. Additionally, FRBs so far are only observed at radio wavelengths with no convincing afterglow emission reported to date. However, X-ray emission contemporaneous with FRB-like radio bursts were detected from SGR 1935+2154, which suggests that at least some FRBs could have prompt X-ray counterparts (Bochenek et al. 2020; CHIME/FRB Collaboration et al. 2020b; Li et al. 2021; Mereghetti et al. 2020; Ridnaia et al. 2021). Such X-ray emission currently can only be detected for nearby FRBs (<50 Mpc; Scholz et al. 2020).

[18] Veni Fellow.
[19] For a complete list of known FRBs, see https://www.herta-experiment.org/frbstats/ or the TNS (Yaron et al. 2020).
[20] See http://frbhosts.org/ (visited on 2021 July 1); Heintz et al. (2020).

Table 1
Properties of the Bursts from FRB 20181030A

TNS Name	MJD	Arrival Time[a] (UTC @ 400 MHz)	S/N[b]	DM_{bb}[c] (pc cm^{-3})	DM[d] (pc cm^{-3})
FRB 20181030A[e]	58421	04:13:13.1758(8)	32.5	⋯	103.5 ± 0.7
FRB 20181030B[e]	58421	04:16:21.6419(14)	17.1	⋯	103.5 ± 0.3
FRB 20200122A	58870	10:20:32.5805(3)	13.9	103.53 ± 0.02	103.40 ± 0.14
FRB 20200122B	58870	10:27:00.4412(3)	17.3	103.49 ± 0.02	103.47 ± 0.08
FRB 20200122C	58870	10:28:20(1)	8.3	⋯	103.1 ± 1.2
FRB 20200122D	58870	22:09:30.8575(3)	13.1	103.58 ± 0.19	103.7 ± 0.4
FRB 20200122E	58870	22:09:52(1)	10.4	⋯	103.27 ± 0.13
FRB 20200122F	58870	22:22:21(1)	8.9	⋯	103.7 ± 0.7
FRB 20200122G	58870	22:23:20.3080(3)	10.5	103.57 ± 0.10	103.7 ± 0.5

Notes.
[a] All burst times of arrival are topocentric. For FRBs 20200122C, 20200122E, and 20200122F, the arrival times are reported by the CHIME/FRB real-time pipeline (CHIME/FRB Collaboration et al. 2018). For FRBs 20200122A, 20200122B, 20200122D, and 20200122G, the arrival times are estimated by the baseband pipeline (Michilli et al. 2021). Finally, the arrival times of FRBs 20181030A and 20181030B are taken from the CHIME/FRB Collaboration et al. (2019).
[b] For all except FRBs 20181030A and 20181030B, band-averaged signal-to-noise ratios (S/Ns) are estimated by the CHIME/FRB real-time pipeline.
[c] S/N-optimized DM for the bursts detected in the baseband data.
[d] S/N-optimized DM from intensity data (see CHIME/FRB Collaboration et al. 2019; Fonseca et al. 2020).
[e] Data from CHIME/FRB Collaboration et al. (2019).

Recently, Bhardwaj et al. (2021) reported the discovery of an FRB with the lowest dispersion measure (DM) observed to date, FRB 20200120E, located toward the outskirts of the nearby spiral galaxy M81. Using the European Very-Long-Baseline Interferometry Network, Kirsten et al. (2021) localized the FRB with subarcsecond precision to an M81 globular cluster. At a distance of 3.6 Mpc, FRB 20200120E is an excellent candidate for multi-wavelength observations that could strongly constrain the nature of the FRB progenitor.

Here we report the identification of the most likely host for FRB 20181030A,[21] a repeating FRB first reported by the CHIME/FRB Collaboration et al. (2019). Though its DM is only 103.5 pc cm^{-3}, this is significantly larger than the expected contribution in this direction from the Milky Way disk ($\sim$33–41 pc cm^{-3}). The CHIME/FRB Collaboration et al. (2019) did not find any Galactic ionized and/or star-forming region in the direction of FRB 20181030A. As a result, they concluded that the FRB should have a nearby extragalactic host. However, due to insufficiently precise localization of the FRB reported by the CHIME/FRB Collaboration et al. (2019), they could not make any firm association with a host. Since that report, CHIME/FRB has detected seven more bursts from the FRB (see Table 1).[22] For several of the FRB repeat bursts, raw voltage data were acquired, enabling localization of the FRB to a few arcminutes precision, an improvement of over a factor of 200 in the localization area. Within this localization region, we identify a local universe spiral galaxy, NGC 3252 (Huchra et al. 1983), as its most likely host.

The paper is organized as follows. In Section 2, we describe our search for the host of FRB 20181030A. From the low chance-coincidence probability (Section 2.1) and absence of any other viable host candidates in the FRB localization region (Section 2.2), we argue that NGC 3252 is a promising host for the FRB. We estimate notable physical properties of NGC 3252 in Section 2.4 and then discuss our archival multi-wavelength data search to identify any FRB plausible counterpart in Section 2.5. In Section 3, we discuss implications of this discovery and conclude in Section 4.

[21] Formerly named FRB181030.J1054+73.
[22] For a complete list, check http://chime-frb.ca/repeaters/FRB20181030A (visited on 2021 July 1).

Table 2
Major Observables of FRB 20181030A

Parameter	Value
R.A.(J2000)[a]	$10^h34^m20^s.1 \pm 30^s.6$
Decl. (J2000)[a]	$73°45'05'' \pm 47''$
l, b	134.°81, +40.°06
DM[b]	103.5 ± 0.3 pc cm^{-3}
$DM_{MW,NE2001}$[c]	41 pc cm^{-3}
$DM_{MW,YMW16}$[c]	33 pc cm^{-3}
$DM_{MW,halo}$[d]	30 pc cm^{-3}
Max. distance[e]	$\lesssim$225 Mpc

Notes.
[a] The 90% confidence localization region of the FRB.
[b] From CHIME/FRB Collaboration et al. (2019).
[c] Maximum DM model prediction along this line of sight for the NE2001 (Cordes & Lazio 2002) and YMW16 (Yao et al. 2017) Galactic electron density distribution models.
[d] Fiducial Milky Way halo prediction from the Dolag et al. (2015) hydrodynamic simulation and Yamasaki & Totani (2020) Milky Way halo model.
[e] Corresponds to the maximum redshift of 0.05 (see Section 2.2).

2. Observations

The Canadian Hydrogen-Intensity Mapping Experiment Fast Radio Burst Project (CHIME/FRB) (CHIME/FRB Collaboration et al. 2018) first discovered two bursts from FRB 20181030A on 2018 October 30 (CHIME/FRB Collaboration et al. 2019). The source's DM is larger than the predicted Galactic contribution in the FRB sight line (see Table 2). After subtracting DM contributions from the Milky Way disk and halo, as shown in Table 2, the DM excess of the FRB is $\sim$30–40 pc cm^{-3}. Using the average Macquart relation (Equation (2) in Macquart et al. 2020), we estimate the redshift of the FRB to be $\sim$0.03–0.04 assuming negligible host DM contribution. This suggests close proximity of the FRB host ($\lesssim$200 Mpc). As of 2021 July 1, seven

more bursts have been detected from the FRB.[22] Interestingly, all seven bursts were clustered in two different epochs on 2020 January 22, separated by ≈12 hr. This suggests a highly non-Poissonian waiting time distribution for the FRB bursts. Fortunately, four FRB 20181030A bursts have baseband data saved by the CHIME/FRB baseband system (bursts with reported DM_{bb} values in Table 1).

The baseband system of CHIME/FRB stores ∼100 ms of channelized voltages around signals of interest (CHIME/FRB Collaboration et al. 2018). We have developed a pipeline to automatically process such baseband data and localize a burst on the sky with a precision of $\sim\frac{8}{S/N}$ arcmin (Michilli et al. 2021). This is achieved by mapping the signal strength with a grid of largely overlapping beams around an initial guess. The resulting S/N measured in each beam is fitted with a mathematical model of the formed beam of the telescope. Systematic effects have been corrected by using a sample of sources with known positions. In this case, we used the baseband data of four detected bursts of FRB 20181030A, FRBs 20200122A, 20200122B, 20200122D, and 20200122G to estimate the localization region of the FRB. The dedispersed baseband data waterfall plots and major characteristics of the four FRB bursts are shown in Figure 1 and Table 1, respectively. Other burst properties, such as fluence and flux density, along with a detailed description of both the intensity and baseband data analysis of all newly discovered FRB 20181030A bursts will be presented elsewhere. Moreover, the available data are insufficient to estimate meaningful constraints on the FRB's periodicity. As the reported baseband localization uncertainties are statistical in nature (Michilli et al. 2021), we combined the localization regions of the four FRB bursts using a weighted average with inverse-variance weights and localized the FRB to a sky area of ≈5.3 $arcmin^2$ (90% confidence region; see Table 2). Next, we use the baseband localization region of FRB 20181030A to search for a potential host galaxy.

2.1. Host Galaxy Search

First, we argue below that the FRB is unlikely to be Galactic in origin. As noted by the CHIME/FRB Collaboration et al. (2019), there is no cataloged Galactic ionized region, satellite galaxy, or globular cluster in the direction of the FRB that could contribute to the FRB DM. Moreover, Ocker et al. (2020) estimated the mean DM through the Milky Way's warm ionized medium at large distances from the Galactic plane ($z > 2$ kpc), $\overline{DM \sin|b|} = 23.0 \pm 2.5$ pc cm^{-3}. At the FRB's Galactic latitude ($b = 40°$), it would give a mean Galactic DM of $\approx 36 \pm 5$ pc cm^{-3}. This agrees well with the prediction of the two Galactic DM models. The Milky Way halo DM contribution, DM_{halo}, however, is poorly constrained. Recently, Kirsten et al. (2021) estimated the Milky Way halo contribution in the direction of FRB 20200120E to be $\lesssim$40 pc cm^{-3}. If this is also true for the FRB 20181030A sight line, the FRB would be clearly extragalactic in origin. However, the halo may be clumpy (Kaaret et al. 2020), so it may still be possible to have significant variations in DM_{halo} along different sight lines. Using the same argument as asserted by Bhardwaj et al. (2021), an FRB with a DM excess of ∼70 pc cm^{-3}, if Galactic, would require a very distant ($\gtrsim$100 kpc) and unusually energetic neutron star as its source. As discussed below, we have found an extragalactic host with a low chance-coincidence probability. Therefore, Occam's razor argues for the extragalactic association.

Next, we searched the NASA Extragalactic Database (NED) for cataloged galaxies within the FRB 90% confidence localization region and found only one galaxy, NGC 3252, with a redshift (z) of 0.00385(2) (Masters et al. 2014). NGC 3252 is a bright ($m_r = 12.58$ AB mag) Scd Hubble-type edge-on spiral galaxy (de Vaucouleurs et al. 1991) at a luminosity distance of ≈20 Mpc. In Figure 2, we plotted the FRB localization region over a Pan-STARRS RGB image made using Pan-STARRS's g-band (B:blue), r-band (G:green), and z-band (R:red) data. In the figure, NGC 3252 is the most prominent galaxy. Note that NED does not provide the depth of completeness of cataloged galaxies in their search results. Therefore, in Section 2.2, we describe our search of dwarf galaxies within the FRB localization region.

We now estimate the chance-coincidence probability (P_{cc}) of finding an NGC-3252-like bright galaxy close to the FRB localization region. Briefly, we assume a Poisson distribution of galaxies across the sky and calculate the probability of finding one or more galaxies with m_r smaller than or equal to that of NGC 3252 (12.79 AB mag; without correcting for the Galactic extinction) by chance close to the FRB 90% confidence localization region (5.3 $arcmin^2$). Using the areal number density of NGC-3252-like or brighter galaxies, $n(m_r \leqslant 12.79) = 0.2$ deg^{-2} from Driver et al. (2016), we estimate $P_{cc} = 4.5 \times 10^{-4}$. However, as the presence of NGC 3252 is inferred post hoc, we have corrected the P_{cc} to account for the problem of multiple testing (also known as the look-elsewhere effect) using the method described by Bhardwaj et al. (2021). After considering all CHIME FRBs that were discovered before the first detected burst of FRB 20181030A and have a DM excess $\leqslant$103.5 pc cm^{-3} (see Figure 3), we estimate the P_{cc} to be <0.0025.

We should point out, however, that our chance-coincidence analysis favors brighter galaxies over fainter ones because the latter are more abundant and therefore more likely to be found in the FRB localization region by chance. Therefore, in the next section, we searched for faint galaxies within the FRB localization region.

2.2. A Dwarf Host of FRB 20181030A?

In order to check if any plausible dwarf galaxy exists within the FRB localization, we first estimated the maximum redshift of the FRB 20181030A host by performing a Markov-Chain Monte Carlo (MCMC) simulation, which is discussed in Appendix A. Using the priors shown in Table 8 and an `emcee` based MCMC inference framework (Foreman-Mackey et al. 2013), we computed a one-sided 95% Bayesian credible upper limit on the FRB host redshift (z_{max}) = 0.05 from the marginalized host redshift posterior.

There are a few factors that make our maximum redshift estimate conservative. If the FRB host lies beyond NGC 3252, the FRB sight line would traverse the NGC 3252 halo with a projected offset $\leqslant$14 kpc. Using the stellar mass of NGC 3252 from Table 6, we estimated its halo mass to be 1.9×10^{11} $M_\odot$ using Equation (2) from Moster et al. (2013), and the NFW profile halo concentration factor = 9.4 using Equation (24) from Klypin et al. (2016). At a projected offset of 14 kpc, using the method described by Bhardwaj et al. (2021), we estimate the DM contribution of the NGC 3252 halo ≈15 or 30 pc cm^{-3} for baryon fractions 0.4 and 0.75, respectively, using the halo-density profile from

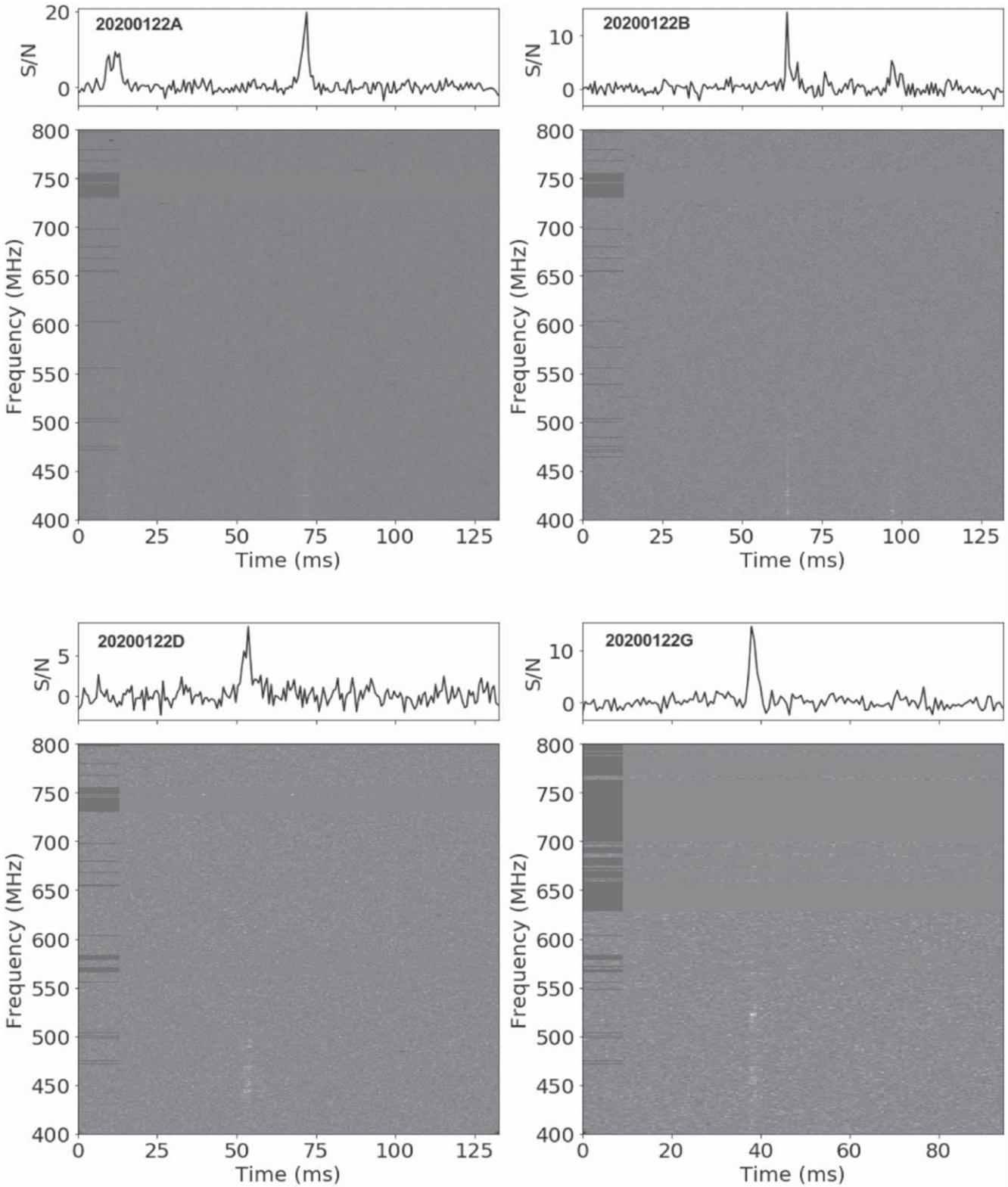

Figure 1. Frequency vs. time ("waterfall") plots of the four dedispersed bursts detected from FRB 20181030A with saved baseband data. See Table 1 for their major burst properties. The waterfall plots are binned to have temporal resolution 0.655 ms and spectral resolution 0.391 MHz. Dark gray lines represent bad frequency channels that were flagged in this analysis. Note that FRBs 20200122A and 20200122B show sub-bursts separated by ∼60 ms and 30 ms, respectively. Detailed analysis of these sub-bursts will be reported elsewhere.

Maller & Bullock (2004) (the profile that predicted the lowest M81 halo DM in Figure 4 of Bhardwaj et al. 2021). The former baryon fraction value is the minimum that Hafen et al. (2019) found in the Feedback In Realistic Environments simulation for a halo of mass $\sim 10^{11}$ $M_{\odot}$). The latter value, i.e., 0.75, is estimated assuming ≈25% of the baryons exist in the galaxy as the interstellar medium (ISM), stars, and compact remnants (Fukugita et al. 1998). Moreover, NGC 3252 is a part of a galaxy group with the dynamic

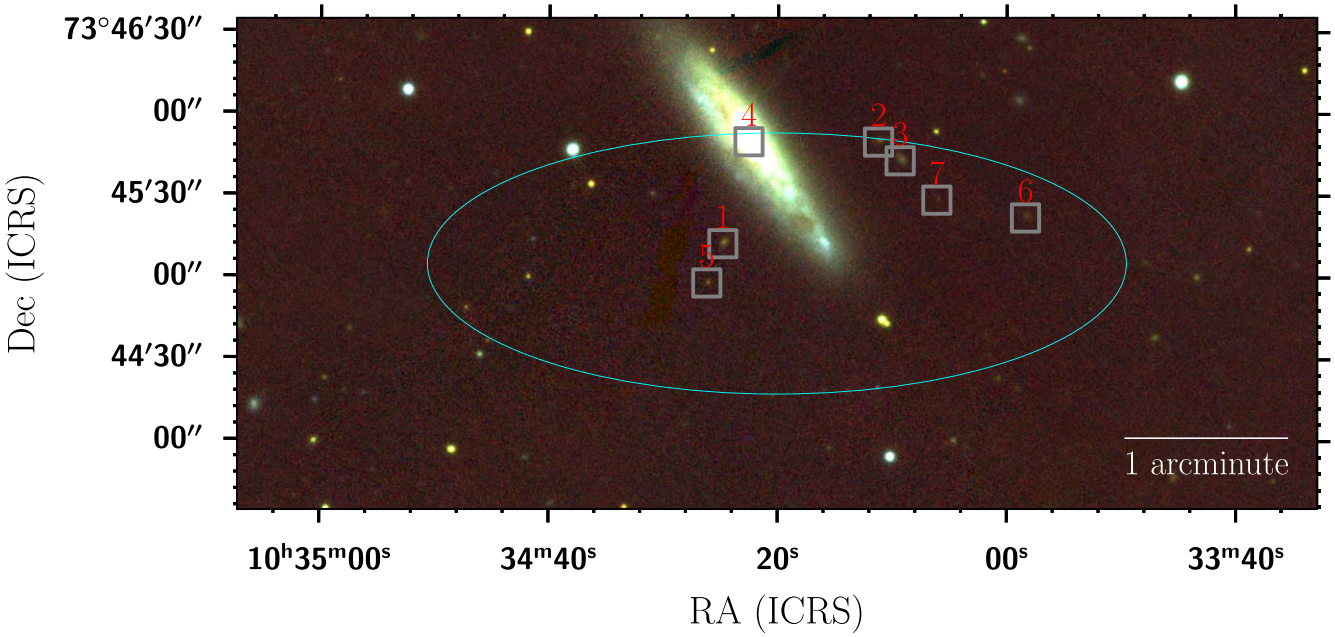

Figure 2. Pan-STARRS RGB-image of the FRB 20181030A 90% localization region (cyan ellipse). Grey boxes show the locations of seven host-galaxy candidates within the localization region (see Table 4); Source 4 is NGC 3252 at $z = 0.0039$, the most promising candidate for host galaxy of the FRB.

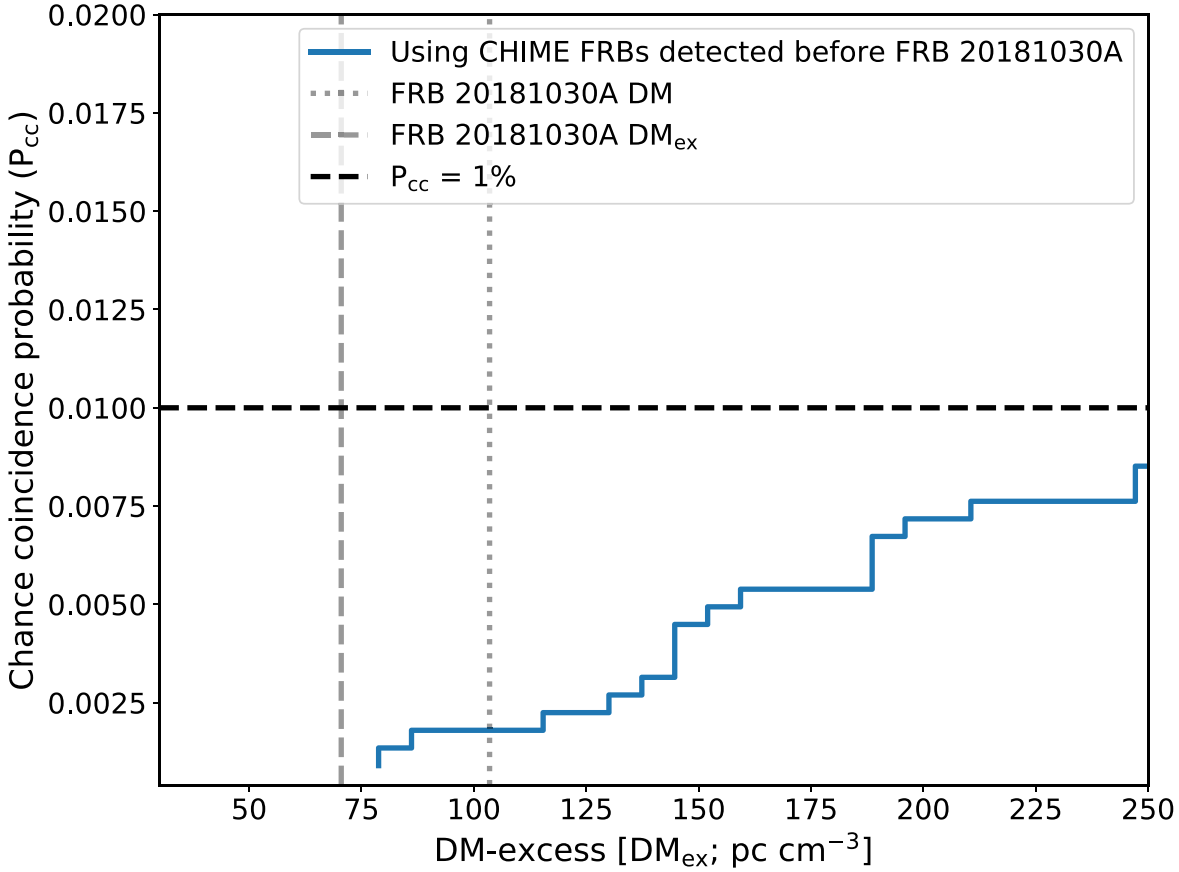

Figure 3. The chance-coincidence probability of finding an NGC-3252-like galaxy as a function of the DM excess (DM_{ex}) of CHIME FRBs detected before the first burst of FRB 20181030A (see Section 2.1). As discussed by Bhardwaj et al. (2021), the latter step takes into account the look-elsewhere effect. Given the DM of FRB 20181030A, 103.5 pc cm^{-3}, $P_{cc} < 0.0025$.

group mass $= 1.2 \times 10^{12}$ $M_{\odot}$ (Kourkchi & Tully 2017). In addition to this, the FRB sight line intersects several other galaxy groups that are located within $z = z_{max}$ (Tempel et al. 2016; Lim et al. 2017). All these would contribute to the observed FRB DM and consequently, if accounted for, would reduce our maximum redshift estimate considerably.

Note that an FRB 20121102A-like star-forming dwarf galaxy ($M_r = -17$ AB mag; Tendulkar et al. 2017), the faintest

Table 3
Log of the GTC/OSIRIS Long-slit and MOS Spectroscopic Observations of the FRB 20181030A 90% Localization Region

Program	Date	Mode	Grism	Position Angle	Exposure Time	Seeing	Airmass	Night
GTC04-20BDDT	2020/10/24	long-slit	R1000B	37°.31	4 × 60 s	1″.2	1.59	Dark
GTC04-20BDDT	2020/10/26	MOS	R500R	0	8 × 700 s	1″.5	1.75	Dark
GTC18-21AMEX	2021/05/04	MOS	R500B	0	3 × 1200 s	0″.9	1.68	Dark
GTC18-21AMEX	2021/05/15	MOS	R500B	0	3 × 1200 s	1″.0	1.56	Dark

Table 4
Galaxies Identified within the FRB Localization Region with $M_r < -15$ AB mag at $z_{max} = 0.05$

Number	R.A. J2000	Decl. J2000	DESI(*r*-band)[a] AB mag.	Identified Lines	z_{spec}
1	$10^h34^m24^s.81$	73°45′12″.81	19.69	[O II], Ca doublet, *G*-band	0.460(1)
2	$10^h34^m11^s.23$	73°45′49″.23	19.89	Ca doublet, *G*-band, Mg, Na	0.455(2)
3	$10^h34^m9^s.33$	73°45′42″.33	19.41	[O II], Ca doublet, [O III] doublet	0.276(2)
4[b]	$10^h34^m22^s.56$	73°45′49″.56	12.58	see text	0.00385(2)
5	$10^h34^m26^s.20$	73°44′57″.20	21.61	Ca doublet, *G*-band, Mg, Na	0.645(1)
6	$10^h33^m58^s.36$	73°45′21″.36	20.76	Ca doublet, *G*-band	0.647(1)
7	$10^h34^m6^s.12$	73°45′28″.12	21.67	[O II], Ca doublet	0.563(2)

Notes.
[a] The *r*-band magnitudes are corrected for the Milky Way extinction.
[b] Source 4 is NGC 3252, and at a spectroscopic redshift = 0.0039 (20 Mpc), it is the only galaxy in our list with a redshift $< z_{max}$.

FRB host discovered to date, if located at z_{max}, would have *r*-band magnitude ≈19.8 AB mag. Fortunately, the FRB field of view is imaged by the Dark Energy Spectroscopic Instrument (DESI) Legacy Imaging Survey (Dey et al. 2019) with an *r*-band depth ≈24 AB mag (5σ). Using the DESI data, Zou et al. (2019) estimated photometric redshifts of all the identified galaxies with a 5σ *r*-band completeness limit of 23.6 AB mag. However, this limit is likely not complete for low-surface-brightness (LSB) galaxies. For the DESI Legacy Imaging Survey, the average *r*-band surface-brightness limit is ∼26 mag arcsec^{-2} (Dey et al. 2019; Arora et al. 2021; Tanoglidis et al. 2021). At $z = z_{max}$, an $M_r = -17$ AB mag LSB galaxy of effective radius ∼1–3 kpc (Greco et al. 2018) and uniform surface brightness = 26 mag arcsec^{-2} should be detected in the DESI data as an $m_r \lesssim 22$ AB mag source. More importantly, the $m_r \lesssim 22$ AB mag limit is sensitive to detecting a dwarf host five times less luminous than any FRB host discovered to date ($M_r = -15$ AB mag). Given this constraint, we selected seven galaxies from Zhou et al. (2020), including NGC 3252, which have $m_r \leqslant 22$ AB mag and are located within the FRB 90% confidence localization region (shown as a cyan ellipse in Figure 2) and estimated their spectroscopic redshifts using the 10.4 m Gran Telescopio Canarias (GTC) (see Section 2.3).

2.3. GTC Observations and Analysis

In this section, we describe our GTC observations of the seven plausible host candidates. As will be shown later, only NGC 3252 satisfies the z_{max} constraint, and hence, is the most plausible host of the FRB.

2.3.1. Observations

Observations of the galaxies identified within the FRB 20181030A 90% localization region were performed with the the Optical System for Imaging and low-intermediate Resolution Integrated Spectroscopy (OSIRIS[23]) at the GTC. The OSIRIS detector consists of two CCDs and provides a field of view (FoV) of 7′.8 × 7′.8 with a pixel scale of 0″.254. The data were obtained during four observing runs in 2020 October and 2021 May. The observing blocks corresponding to the first two runs were executed under Director's Discretionary time. A summary of the observations is given in Table 3.

We obtained long-slit spectra of the NGC 3252 using the R1000B grism that covers the spectral range from 3700 to 7500 Å, with the 1″.2 slit width, providing a spectral resolution of about 9 Å. The slit was placed to pass through the major axis of the galaxy at a P.A. = 37°.31, which is shown in Figure 7.

To perform simultaneous observations of the other six host galaxy candidates in the localization region (see Table 4), we utilized the OSIRIS MOS (multi-object spectroscopy) mode. The mask for the MOS observations was designed with the OSIRIS Mask Designer Tool (González-Serrano et al. 2004; Gómez-Velarde et al. 2016) using the catalog coordinates of the galaxies and a set of five fiducial stars. The observations were performed with the R500B and R500R grisms that cover the spectral ranges 3600−7200 Å and 4800−10000 Å, respectively. For the target galaxies we designed rectangular slitlets with length varying between 4″.5 and 10″ and a width of 1″.5 each. Two additional slitlets covered source-free regions for sky subtraction. The spectral resolution of the R500B and R500R data is ∼21 Å and ∼27 Å, respectively.

2.3.2. Data Reduction

The OSIRIS MOS and long-slit spectra were reduced using the GTCMOS pipeline (Gómez-González et al. 2016) and standard IRAF routines (Tody 1986, 1993). All spectra were bias-subtracted and flat-fielded using the set of corresponding images taken during the same observing nights. For flux

[23] http://www.gtc.iac.es/instruments/osiris/

Table 5
Galaxies with $m_r > 22$ AB mag in the FRB 90% Confidence Localization Region

Number	R.A. J2000	Decl. J2000	DESI(r-band) AB mag.	$z_{\rm photoz}$ [a]	$z_{\rm photoz\text{-}err}$ [a,b]
1	$10^{\rm h}34^{\rm m}16\overset{\rm s}{.}01$	73°44′18.″60	22.56	0.62	0.06
2	$10^{\rm h}33^{\rm m}59\overset{\rm s}{.}30$	73°44′40.″56	22.90	0.60	0.09
3	$10^{\rm h}34^{\rm m}35\overset{\rm s}{.}06$	73°44′58.″56	22.73	0.72	0.06

Notes.
[a] From photometric redshift catalog of galaxies detected in the DESI survey (Zou et al. 2019).
[b] For all three galaxies, $z_{\rm photz} - 5\sigma_{\rm photz-err} > z_{\rm max}$.

calibration we used spectrophotometric standards Feige 110, GD153, and Ross 640 (Oke 1974, 1990; Bohlin et al. 1995) observed during the same nights as the targets. A set of arc-lamp spectra of Ne, Hg, and Ar was used for wavelength calibration. The rms errors of the resulting solutions were <0.5 Å for the R1000B grating and <2 Å for the R500R and R500B gratings.

2.3.3. Multi-object Spectroscopy

The resulting product of the pipeline contained 2D calibrated spectra collected in all of the slitlets. We extracted each spectrum and subtracted the sky using the IRAF task *apall*. We utilized background from the source-free regions to subtract sky from the spectra obtained in the shortest slitlets. The lines identified for each galaxy and the corresponding average redshifts are presented in Table 4. To confirm our redshift estimations, we used the Manual and Automatic Redshifting Software (MARZ, Hinton et al. 2016) and compared the extracted spectra with the galaxy templates. In all cases the identified spectral lines (see Table 4) have shown an agreement with the spectral features corresponding to early-type absorption and intermediate-type galaxy templates, confirming our estimations.

Among the identified host galaxy candidates, only NGC 3252 has a spectroscopic redshift $<z_{\rm max}$. This makes NGC 3252 the only viable FRB host candidate among all the identified galaxies with $m_r \leqslant 22$ AB mag. Note that blue star-forming dwarf galaxies have been proposed to host FRB progenitors (Metzger et al. 2017) via "prompt" formation channels, such as superluminous supernovae and long gamma-ray bursts (Fruchter et al. 2006). However, because of their highly dynamic and rich ISM, these galaxies are expected to contribute significantly to the FRB DM (Li et al. 2019). For instance, Tendulkar et al. (2017) estimated that the DM contribution of the FRB 20121102A host, a dwarf irregular star-forming galaxy, is ∼60–220 pc cm^{-3}. Hence, together with the inference from Section 2.2, the prospect of a host galaxy beyond NGC 3252 seems unlikely. Lastly, in Table 5, we have listed the three galaxies in the photometric redshift catalog of DESI extragalactic sources (Zou et al. 2019) that are located within the FRB localization region and have r-band magnitude >22 AB mag along with their estimated photometric redshifts. All three galaxies have 5σ lower limit on the redshift $>z_{\rm max}$. Therefore, we conclude that the association between FRB and NGC 3252 is real and robust.

2.4. Physical Properties of NGC 3252

Here we summarize major physical properties of NGC 3252. We obtained long-slit spectroscopy data from GTC and its analysis is described in Appendix B. From the integrated optical spectrum of the galaxy, we estimate the oxygen abundance $12+\log({\rm O/H}) = 8.44 \pm 0.06$ (or nebular metallicity $\log(Z_{\rm gas}/Z_\odot) = -0.25 \pm 0.07$), which is ∼60% of the solar value (Asplund et al. 2009). We also derive dust extinction at the V-band, $A_v = 1.3 \pm 0.2$ ($E(B-V) = 0.42 \pm 0.06$ using $R_v = 3.1$), using Hα/Hβ ratio (i.e., Balmer decrement), assuming the standard Milky Way extinction curve (Cardelli et al. 1989). Finally, using ${\rm SFR(H}\alpha) = 7.9 \times 10^{-42}\ M_\odot\ {\rm yr}^{-1} \times L({\rm H}\alpha/{\rm erg\ s}^{-1})$ (Kennicutt et al. 1994), we get ${\rm SFR(H}\alpha) = 0.033\ M_\odot\ {\rm yr}^{-1}$ using the extinction-corrected total Hα luminosity of $L({\rm H}\alpha) = 4.12 \times 10^{39}$ erg s^{-1}.

However, as the slits only cover a small fraction of the surface area of NGC 3252, it is expected that the above star formation rate is significantly underestimated. Therefore, we estimate the total star formation rate ($\rm SFR_{total}$) by combining the total infrared (TIR) luminosity and far-UV- (FUV-) derived SFR as described in Iglesias-Páramo et al. (2006), which is found to be a robust estimate for the disk galaxies (Buat et al. 2007). We estimated the TIR luminosity of NGC 3252 using the prescription of Dale & Helou (2002) which uses the Infrared Astronomical Satellite (IRAS) filters' fluxes (Fullmer & Londsale 1989), and got $L({\rm TIR}) = 2.13 \times 10^9\ L_\odot$. Using Equation (5) from Iglesias-Páramo et al. (2006), ${\rm SFR(TIR)} = 0.38\ M_\odot\ {\rm yr}^{-1}$. Similarly, for the FUV luminosity, we use the Galex NUV filter flux and estimated the ${\rm SFR(FUV)} = 0.13\ M_\odot\ {\rm yr}^{-1}$ using the extinction-uncorrected L(FUV) of NGC $3252 = 2.7 \times 10^8\ L_\odot$. Finally, the total recent star formation rate was calculated using the relation from Iglesias-Páramo et al. (2006): $\rm SFR_{total} = SFR(NUV) + (1-\eta) \times SFR(TIR) = 0.36\ M_\odot\ yr^{-1}$ where $\eta = 0.4$ for disk galaxies in the local universe (Iglesias-Páramo et al. 2004), which accounts for the fraction of the total IR luminosity heated by old stars. This relation has a calibrated uncertainty of about 20%.

To estimate stellar mass, metallicity, and mass-weighted age of NGC 3252, we use a Bayesian inference spectral energy distribution (SED) fitting code, `Prospector` (Leja et al. 2017; Johnson et al. 2019). Appendix C describes the SED fitting analysis in detail. We used 17 broadband filter fluxes covering the FUV band to far-infrared (FIR) bands (see Table 10) of NGC 3252 and fit a five-parameter delayed-τ model (Simha et al. 2014; Carnall et al. 2019). This model and assumed priors of the free parameters are discussed in Appendix C. The best-fit SED profile of NGC 3252 is shown in Figure 4. `Prospector` also allows for MCMC posterior sampling to estimate uncertainty in the best-fit values of the model parameters, which are stated in Table 6.

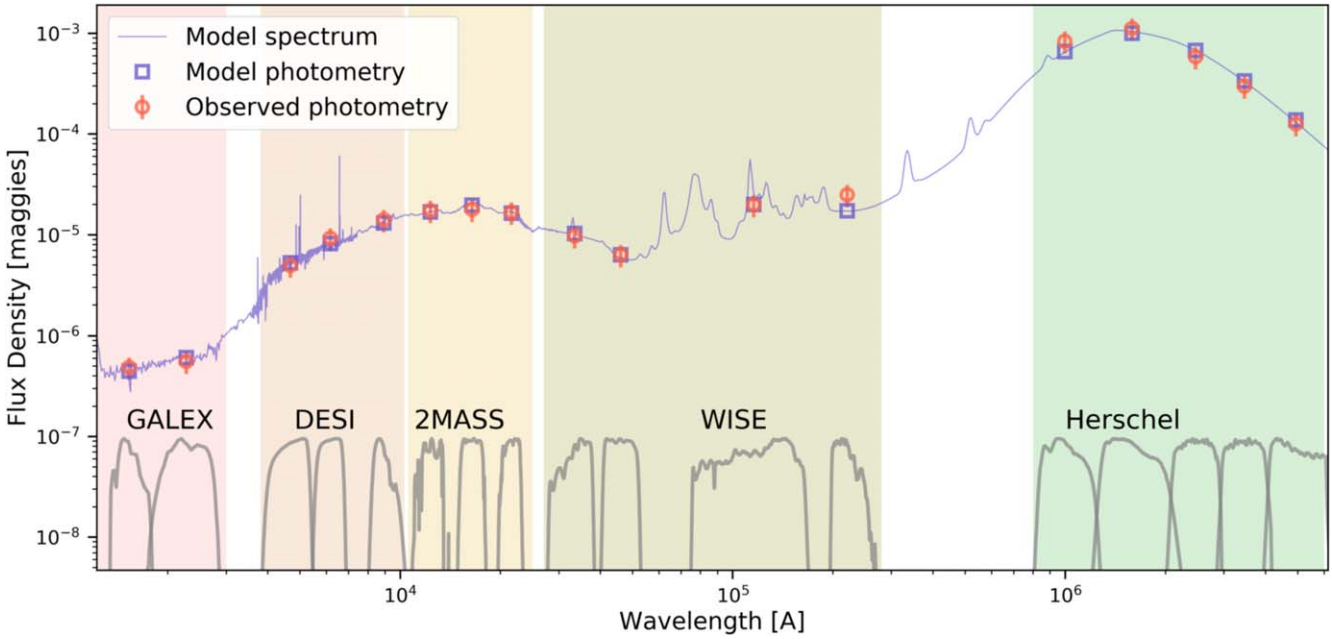

Figure 4. Modeling the SED of NGC 3252. The flux density of NGC 3252 in different wavelength bands are plotted along with the best-fit `Prospector` model spectrum. To assess the quality of the `Prospector` model, the modeled and actual photometry data are also shown. The shown model profile is used to estimate different physical properties of NGC 3252. For more information, see Appendix C. The modeled SED of NGC 3252 shown in Figure 4 is in excellent agreement with that of a typical star-forming galaxy (Leitherer 2005).

Table 6
Notable Properties of NGC 3252

Property	Value	References
log[SFR] ($M_\odot$ yr^{-1})	-0.45 ± 0.1	this work
Stellar metallicity (log($Z/Z_\odot^a$))[a]	$-0.21^{+0.18}_{-0.19}$	this work
Nebular metallicity (log($Z_{gas}/Z_\odot$))	-0.25 ± 0.07	this work
Oxygen abundance [O/H]	8.44 ± 0.06	this work
Stellar mass ($M_\odot$)	$5.8^{+1.6}_{-2.0} \times 10^9$	this work
Effective radius (R_{eff}; kpc)	2.6	Salo et al. (2015)
Mass-weighted age (Gyr)	$4.8^{+1.6}_{-1.8}$	this work
$E(B-V)$ (mag)	0.42 ± 0.06	this work
Absolute r-band mag. (AB)	-19.1 ± 0.5	...
Luminosity distance (Mpc)	20 ± 5	Tully et al. (2016)

Note.
[a] Estimated using PROSPECTOR; see Appendix C.

2.5. Search for a Multi-wavelength Counterpart to FRB 20181030A

2.5.1. Persistent Radio Source Search

We searched archival radio data of the following surveys to check for the presence of a persistent radio source within the FRB uncertainty region: the NRAO VLA Sky Survey (NVSS; Condon et al. 1998), the VLA Sky Survey (Lacy et al. 2016, VLASS), the Westerbork Northern Sky Survey (WENSS; Rengelink et al. 1997), and the Tata Institute of Fundamental Research Giant Metrewave Radio Telescope Sky Survey (TGSS) Alternative Data Release (Intema et al. 2017). We found only one radio source, NVSS J103422+734554. The radio source is only detected in NVSS and is either unresolved or marginally extended. Moreover, it is spatially coincident with the center of NGC 3252. Table 7 lists 5σ upper limits on the source's integrated flux density derived from the archival radio images of all other surveys. The NVSS radio source is likely resolved out and hence, undetected in the VLASS 2.1 data. In VLASS 1.1 data, we detected an irregular-shaped source spatially coincident with the NVSS radio source. However, due to the lack of detection in the VLASS 2.1 data despite similar sensitivity and known calibration and imaging artifacts in the VLASS 1.1 data (Lacy et al. 2016), the radio source is likely spurious (M. Lacy 2021, private communication). From the non-detection in the TGSS data and assuming a power-law dependence of the NVSS radio-source flux density, i.e., $S_\nu \propto S^\alpha$, we estimated a lower limit on $\alpha > -0.43$. This agrees well with the observed radio continuum spectral index of local star-forming galaxies (between -0.1 and -0.7; Marvil et al. 2015).

While searching the VLA archive, we also found raw EVLA data (project ID = AK752) that cover the FRB localization region. Observations were conducted on 2010 June 19 (MJD 55366) with the array in D-configuration in two 128 MHz bandwidth sub-bands with central frequencies 4.495 and 7.852 GHz and about 40 minutes of time on source. The absolute flux density calibrator 3C 147 and the phase calibrator J1048+7143 were used. The data were calibrated and flagged using `CASA` software (McMullin et al. 2007). Additional RFI flagging and self-calibration were done resulting in a final primary beam corrected image with a local rms noise of $\sigma \approx 30\ \mu$Jy beam^{-1}. Within the FRB localization region, we detect only the NVSS radio source extended in both the EVLA observations (see Figure 5). The integrated flux density of the NVSS source at 4.495 and 7.852 GHz is estimated using the `Aegean` package (Hancock et al. 2012, 2018) and is stated in Table 7. Using the EVLA flux densities at 4.495 and 7.852 GHz, we estimated α to be -0.94 ± 0.16, which is steeper than the lower limit on α estimated using the flux densities at 150 MHz and 1.4 GHz (>-0.43). This is not unusual as the radio spectra of star-forming galaxies are known to show a break (or an exponential

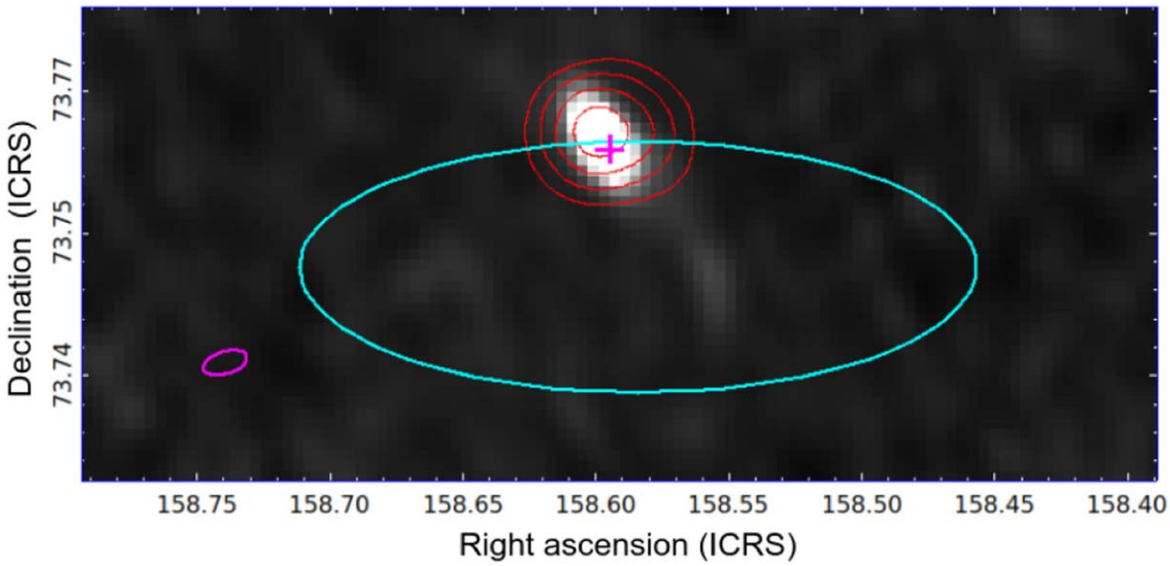

Figure 5. The EVLA 4.5 GHz image of the FRB 20181030A 90% localization region (cyan ellipse). NVSS contours (3, 2.5, 2, and 1.5 mJy) of the radio source are shown in red. The center of NGC 3252 (see Table 4) is represented by a magenta cross. Finally, the EVLA beam is shown as a magenta ellipse on the bottom left side of the image.

Table 7
Summary of Radio Observations of NGC 3252

Survey	Frequency (GHz)	Date (UT)	Image Resolution[a] ($''$)	Integrated Flux Density (mJy)
TGSS	0.15	2016 Mar 15	25	<10[b]
WENSS	0.326	1997 Oct 22	56	<18[b]
NVSS[c]	1.4	1993 Dec 18	45	3.8 ± 0.5
VLASS 2.1	3.0	2020 Oct 13	2.5	<0.6[b]
EVLA[c]	4.495	2010 Jun 19	12.8	1.35 ± 0.06
	7.852	2010 Jun 19	9.1	0.80 ± 0.06

Notes.
[a] For each survey, the average of major and minor axes of the formed beam is quoted.
[b] $5\times$ local rms noise.
[c] The lone radio source in the FRB uncertainty region is extended and spatially coincident with the center of NGC 3252 in the NVSS and two EVLA observations.

decline) in the frequency range of 1−12 GHz (Klein et al. 2018)

The NVSS source is likely to be produced via ongoing star formation in NGC 3252. To test this, we estimate the SFR using the NVSS 1.4 GHz continuum emission and compare it with the value estimated in Appendix B. Using the 1.4 GHz–SFR relation from Davies et al. (2017), $\log(\mathrm{SFR}_{\mathrm{UV+TIR}}/M_{\odot}\,\mathrm{yr}^{-1}) = 0.66 \pm 0.02 \times \log(L_{1.4}(\mathrm{W\,Hz}^{-1})) - 14.02 \pm 0.39$, we estimate $\log(\mathrm{SFR}_{\mathrm{UV+TIR}}/M_{\odot}\,\mathrm{yr}^{-1}) = -0.6 \pm 0.5$ which agrees with the SFR estimate in Table 6. Though it is difficult to rule out the presence of a low-luminosity active galactic nucleus (AGN) at the center of NGC 3252 (Maoz 2007), the extended nature of the radio source and agreement of its 1.4 GHz flux density with the SFR of NGC 3252 suggest that an AGN is unlikely to be the dominant source of the observed persistent radio emission. Moreover, from the non-detection of a persistent compact radio source (<0.3 kpc at 20 Mpc) in the FRB 20181030A localization region in the VLASS 2.1 data (which has the best angular resolution among all the radio surveys considered here), we estimate a 3σ upper limit of 480 μJy at 3 GHz which at 20 Mpc implies an isotropic spectral luminosity $\approx 2 \times 10^{26}$ erg s^{-1} Hz^{-1}, at least 1500 times fainter than that of the persistent radio source detected spatially coincident to FRB 20121102A (Chatterjee et al. 2017; Resmi et al. 2020).

2.5.2. Archival Search for X-Ray Counterparts

We searched the Transient Name Server (TNS)[24] for any archival transient event that is spatially and temporally coincident with any of the nine recorded FRB 20181030A bursts and found none. We also checked if the FRB was visible to the Swift/Burst Alert Telescope (BAT) and Fermi/GBM at the time of the bursts. Unfortunately, Swift/BAT was either not operational (transiting through the South Atlantic Anomaly region) or the FRB location was not within the BAT's field of view. Similarly, for all except FRB 20200122A, the FRB location was not visible to Fermi/GBM. If FRB 20200122A was associated with a giant magnetar flare like the one detected from SGR 1806−20 on 2004 December 27 (Palmer et al. 2005), Fermi/GBM with a flux sensitivity of $\sim 10^{-7}$ erg cm^{-2} s^{-1} in the 50–300 keV band (von Kienlin et al. 2020) would have marginally detected it. This places an upper limit on the

[24] https://www.wis-tns.org/

coincident X-ray flare energy $\approx 10^{46}$ erg s^{-1} at 20 Mpc (without correcting for the attenuation by the host).

There is an X-ray source RX J1034.3.3+7345 (or 1AXG J103422+7344 in the *ASCA* medium sensitivity survey by Ueda et al. 2001) in the vicinity of NGC 3252. This source was discovered in the ROSAT all-sky survey (Truemper 1982) and was initially associated with NGC 3252 by Bade et al. (1998), Condon et al. (1998), and Bauer et al. (2000). However, with the availability of higher-resolution X-ray images, this association has been argued to be incorrect (Haakonsen & Rutledge 2009). More interesting, the X-ray source was found to be spatially coincident with an optical transient PTF10hjz discovered by the Palomar Transient Factory (PTF) on 2010 May 16 (Kasliwal 2011). Based on its high optical and radio flux variability and estimated broadband SED, PTF10hjz was later classified as a background blazar (S. Kulkarni 2021, private communication). Therefore, we conclude that the X-ray source RX J103423.1+734525 (or PTF10hjz) is unrelated to FRB 20181030A.

3. Discussion

3.1. Constraints on the Milky Way Halo DM Contribution

With NGC 3252 as its host, we can use FRB 20181030A and its low DM excess (as for FRB 20200120E; Bhardwaj et al. 2021) to constrain the Milky Way halo DM along the FRB sight line. At 20 Mpc, using the average Macquart relation, we estimate $\mathrm{DM_{IGM}} \approx 5$ pc cm^{-3}.[25] Assuming negligible host DM contribution, we find an upper limit on the $\mathrm{DM_{MW,halo}}$ to be 58 and 66 pc cm^{-3} using the $\mathrm{DM_{MW}}$ estimate from the NE2001 and YMW16 models, respectively (see Table 2). However, a negligible host contribution is likely an overly conservative assumption as even in the extreme scenario where the FRB has a very large offset from the host, the host's circumgalactic medium would still contribute to the FRB DM. Therefore, we use the MCMC analysis discussed in Appendix A, but this time, fix the redshift of the FRB to that of NGC 3252. From this analysis, we estimate the $\mathrm{DM_{MW,halo}}$ 90% Bayesian credible interval to be (19, 55 pc cm^{-3}). This, along with a similar constraint derived by Bhardwaj et al. (2021), suggests that the Milky Way halo DM contribution could be relatively small. This in turn would help in constraining the state and composition of the Milky Way circumgalactic medium (Tumlinson et al. 2017). However, to constrain the average $\mathrm{DM_{MW,halo}}$ estimate, we need more low DM FRBs.

3.2. Comparison with SGR 1935+2154 Radio Bursts

From Table 2 of CHIME/FRB Collaboration et al. (2019), the peak 400–800 MHz flux densities of the two published bursts from this source, FRBs 20181030A and 20181030B, are 3.2 ± 1.7 Jy and 3.1 ± 1.4 Jy, respectively. At a distance of 20 Mpc, the isotropic radio luminosity of these two bursts would be $\sim 9 \times 10^{38}$ erg s^{-1}, around six times larger than those of the very bright SGR 1935+2154 radio bursts recently detected by CHIME/FRB and STARE2 (Bochenek et al. 2020; CHIME/FRB Collaboration et al. 2020b).[26] This suggests a continuum of FRB luminosities, at least at low values. Bochenek et al. (2020) estimated the volumetric rate of SGR 1935+2154-like bursts to be $7^{+9}_{-6} \times 10^7$ Gpc^{-3} yr^{-1}, assuming that the FRB luminosity function follows a power law and the FRB rate is proportional to the star formation rate. As at least the two FRB bursts in the first CHIME/FRB catalog (The CHIME/FRB Collaboration et al. 2021) have isotropic luminosity $\geqslant 10^{38}$ erg s^{-1}, we estimate a lower limit on the volumetric rate of FRBs ($\geqslant 10^{38}$ erg s^{-1}) to be $1.5^{+1.6}_{-0.7} \times 10^7$ Gpc^{-3} yr^{-1}. This lower limit is in agreement with the estimate by Bochenek et al. (2020), which supports their conclusion that magnetars like those observed in the Milky Way could be a dominant channel of FRB production, at least at the lower end of the FRB luminosity function. Moreover, the estimated CHIME/FRB volumetric rate agrees with the rate calculated by extrapolating the luminosity function derived from a sample of bright FRBs observed at 1.4 GHz by the Australian Square Kilometre Array Pathfinder and Parkes down to the luminosity of FRB 20181030A's bursts (Lu & Piro 2019; Luo et al. 2020). Lastly, the estimated FRB volumetric rate at low luminosities is at least 100 times higher than the observed volumetric rate of core-collapse supernovae in the local universe (Taylor et al. 2014, $\sim 10^5$ Gpc^{-3} yr^{-1}). Assuming core-collapse supernovae are the most common way to produce compact objects, FRBs detected at low luminosities ($\sim 10^{38}$ erg s^{-1}) are therefore more likely to be repeating sources.

3.3. Implications for Different Progenitor Models

Three repeating FRB sources within a comoving volume out to a distance of 20 Mpc (Bochenek et al. 2020; CHIME/FRB Collaboration et al. 2020b; Bhardwaj et al. 2021) have now been discovered. Using these discoveries, we estimate a lower limit on the comoving number density (n_{FRB}) of repeating FRB sources to be $9^{+7}_{-4} \times 10^4$ Gpc^{-3}. We can also express $n_{\mathrm{FRB}} = R_{\mathrm{FRB}} \tau \eta \zeta$, where R_{FRB} is the local universe volumetric birthrate of repeating FRB sources, τ and ζ are the average lifetime and active-duty cycle of repeating FRBs, respectively, and η is the beaming fraction. Taking the fiducial values of $\eta = 0.1$ and $\zeta = 0.3$ from Lu & Kumar (2016) and Nicholl et al. (2017), we estimate $R_{\mathrm{FRB}} \tau = 3^{+2}_{-1} \times 10^6 \left(\frac{0.1}{\eta}\right) \times \left(\frac{0.3}{\zeta}\right)$ Gpc^{-3}. One of the popular proposed repeating FRB models is a highly magnetized ($>10^{15}$ G) young neutron star with period $\sim$ ms. Nicholl et al. (2017) estimated the volumetric birthrate of millisecond magnetars (R_{ms}) to be $\sim$few 10–100 Gpc^{-3} yr^{-1}. Using this R_{ms} value as R_{FRB}, we estimate $\tau \sim 10^4$–10^5 yr. This is around two orders of magnitude greater than the expected typical lifetime of a repeating FRB in the models that invoke millisecond magnetars ($\sim$30–300 yr; Metzger et al. 2017, 2019). Therefore, it is unlikely that all repeating FRBs are produced by millisecond magnetars formed primarily via cataclysmic events, like superluminous supernovae, or long and short gamma-ray bursts. Note that Nicholl et al. (2017) did not include accretion-induced collapse (AIC) as a channel for forming millisecond magnetars in their calculation due to the high uncertainty in the AIC rates. However, theoretically estimated rates of AIC are found to be comparable to that of binary neutron star mergers (Tauris et al. 2013; Kwiatkowski 2015). If these estimates are correct, including them would not change our conclusion significantly.

[25] $\mathrm{DM_{IGM}}$ is expected to be considerable as the FRB sight line intersects several foreground groups, including that of M81 (Tully 2015) making $\mathrm{DM_{IGM}} = 5$ pc cm^{-3} a conservative estimate.

[26] Assuming the distance to SGR 1935+2154 is 10 kpc, but note that Zhou et al. (2020), Mereghetti et al. (2020), and Bailes et al. (2021) argue for a significantly smaller distance to the magnetar, $\approx$2–7 kpc.

3.4. Comparison with Other Repeating FRB Hosts

With the inclusion of FRB 20181030A, likely localized to the star-forming galaxy NGC 3252, in the sample of five repeating FRBs, 20121102A, 20180916B, 20190711A, 20200120E, and FRB 20201124A (CHIME/FRB Collaboration 2021; Fong et al. 2021; Ravi et al. 2021), it is evident that the repeating FRB hosts exhibit a continuum of properties in terms of their luminosities, stellar masses, metallicity, and SFRs, ranging from FRB 20121102A, a metal-poor, high-star-forming dwarf irregular galaxy, to FRB 20200120E, a metal-rich massive early-type spiral galaxy. However, it is interesting to note that all five localized repeating FRBs discovered thus far are in either spiral or irregular galaxies (Mannings et al. 2021; Bhardwaj et al. 2021), where practically all core-collapse supernovae (SN II, IIn, IIb, and Ib/c) occur (van den Bergh et al. 2005). However, FRB 20200120E is localized to an M81 globular cluster (Kirsten et al. 2021) where core-collapse supernovae are not expected to occur. Therefore, we need a larger sample of FRB hosts to decipher the nature of FRB progenitors. Lastly, we note that all three local universe repeating FRBs have thus far been observed to produce only low-energy bursts ($\lesssim 10^{35}$ erg) unlike, for example, the FRB 20121102A bursts, which have shown a range of burst energies (10^{36}–10^{40} erg; e.g., Chatterjee et al. 2005; Gourdji et al. 2019). More bursts, particularly high-energy ones, from these FRBs would aid in constraining the emission mechanism of the local universe FRBs (Lyubarsky 2021).

4. Summary and Conclusions

We have reported on the likely association of the repeating FRB 20181030A discovered by CHIME/FRB Collaboration et al. (2019) with a nearby star-forming spiral galaxy, NGC 3252, at a distance of 20 Mpc. The chance-coincidence probability of finding NGC 3252 within the FRB localization region is $<2.5 \times 10^{-3}$. Moreover, we searched for plausible host galaxies within the 90% confidence localization region of the FRB, and found no galaxy except NGC 3252 with $M_r < -15$, a limit in luminosity over five times smaller than for any FRB hosts identified to date.

NGC 3252 is a star-forming spiral galaxy (see Figure 4). We found no archival transient event spatially or temporally coincident with any of the reported FRB 20181030A bursts to date. For one FRB burst, FRB 20200122A, which was detected on 2020 January 22 by CHIME/FRB and was also visible to Fermi/GBM, we estimated an upper limit on the coincident X-ray flare energy to be $\approx 10^{46}$ erg s^{-1}. We also searched for a compact, persistent radio continuum source within the FRB localization region and found none. We then estimated a 3σ upper limit at 3 GHz $= 4.3 \times 10^{25}$ erg s^{-1} Hz^{-1}, at least 1500 times fainter than the persistent source associated with FRB 20121102A. Due to its low DM excess, we constrain the Milky Way halo DM contribution to be 19−55 pc cm^{-3} (90% confidence interval) along the FRB sight line. We also compared the two published FRB 20181030A bursts with those of SGR 1935+2154. The FRB bursts' isotropic luminosity is ∼6 times larger than those of SGR 1935+2154; using this, we have estimated a lower limit on the volumetric rate of FRBs with luminosities $\geqslant 10^{38}$ erg s^{-1}. We found this to be in good agreement with the rate estimated by Bochenek et al. (2020) using the SGR 1935+2154 radio burst, suggesting that many low-luminosity FRBs could be produced by magnetars. Lastly, we also showed that it is unlikely that most of the repeating FRB progenitors are young millisecond magnetars and that if we expect millisecond magnetars to be a source of repeating FRBs, we need multiple repeating FRB formation channels.

At a distance of 20 Mpc, FRB 20181030A is one of the closest FRBs discovered to date. In principle, it should be possible to detect prompt multi-wavelength counterparts as predicted by several FRB models (Yi et al. 2014; Burke-Spolaor 2018; Chen et al. 2020; Nicastro et al. 2021). Therefore, we strongly encourage multi-wavelength follow-up of FRB 20181030A.

We thank the anonymous reviewer and ApJL data editor for their careful reading of our manuscript and their insightful comments and suggestions. We also express our gratitude to Dr. Mark Lacy for the useful discussion related to the VLASS 1.1 data. We thank the Dominion Radio Astrophysical Observatory, operated by the National Research Council Canada, for gracious hospitality and expertise. We acknowledge that CHIME is located on the traditional, ancestral, and unceded territory of the Syilx/Okanagan people. CHIME is funded by a grant from the Canada Foundation for Innovation (CFI) 2012 Leading Edge Fund (Project 31170) and by contributions from the provinces of British Columbia, Québec, and Ontario. The CHIME/FRB Project is funded by a grant from the CFI 2015 Innovation Fund (Project 33213) and by contributions from the provinces of British Columbia and Québec, and by the Dunlap Institute for Astronomy and Astrophysics at the University of Toronto. Additional support was provided by the Canadian Institute for Advanced Research (CIFAR), McGill University and the McGill Space Institute via the Trottier Family Foundation, and the University of British Columbia. The Dunlap Institute is funded through an endowment established by the David Dunlap family and the University of Toronto. Research at Perimeter Institute is supported by the Government of Canada through Industry Canada and by the Province of Ontario through the Ministry of Research & Innovation. FRB research at UBC is supported by an NSERC Discovery Grant and by the Canadian Institute for Advanced Research. The CHIME/FRB baseband system is funded in part by a Canada Foundation for Innovation John R. Evans Leaders Fund award to I.H.S. The National Radio Astronomy Observatory is a facility of the National Science Foundation (NSF) operated under cooperative agreement by Associated Universities, Inc. Based on observations made with the GTC telescope, in the Spanish Observatorio del Roque de los Muchachos of the Instituto de Astrofísica de Canarias, under Director's Discretionary Time. Based on observations made with the Gran Telescopio Canarias (GTC), installed at the Spanish Observatorio del Roque de los Muchachos of the Instituto de Astrofísica de Canarias, in the island of La Palma. This research has made use of the NASA/IPAC Extragalactic Database (NED), which is operated by the Jet Propulsion Laboratory, California Institute of Technology, under contract with the National Aeronautics and Space Administration.

M.B. is supported by an FRQNT Doctoral Research Award. D.M. is a Banting Fellow. T.D.M. is grateful to CONACYT for the research grant CB-A1-S-25070. V.M.K. holds the Lorne Trottier Chair in Astrophysics & Cosmology, a Distinguished James McGill Professorship, and receives support from an NSERC Discovery Grant (RGPIN 228738-13) and Gerhard Herzberg Award, from an R. Howard Webster Foundation Fellowship from CIFAR, and from the FRQNT Centre de

Recherche en Astrophysique du Quebec. B.M.G. is supported by an NSERC Discovery Grant (RGPIN-2015-05948) and by the Canada Research Chairs (CRC) program. C.L. was supported by the U.S. Department of Defense (DoD) through the National Defense Science & Engineering Graduate Fellowship (NDSEG) Program. M.M. is supported by an NSERC PGS-D award. E.P. acknowledges funding from an NWO Veni Fellowship. P.S. is a Dunlap Fellow and an NSERC Postdoctoral Fellow. K.S. is supported by the NSF Graduate Research Fellowship Program.

Facilities: CHIME, Fermi, GTC, VLA.

Software: Prospector (Leja et al. 2017; Johnson et al. 2019), FSPS (Conroy et al. 2009), MARZ (Hinton et al. 2016), CASA (McMullin et al. 2007), Aegean (Hancock et al. 2012, 2018), emcee (Foreman-Mackey et al. 2013), IRAF (Tody 1986, 1993), Fermi GBM data tools (Goldstein et al. 2021), Astropy (Astropy Collaboration et al. 2013, 2018), ALPpy (Robitaille & Bressert 2012), SAOImage DS9 (Joye & Mandel 2003), NumPy (Harris et al. 2020), Matplotlib (Hunter 2007).

Appendix A
MCMC Simulation

We performed an MCMC simulation to estimate the maximum redshift of FRB 20181030A. We used a likelihood defined by the relation, $\mathrm{DM_{FRB}} = \mathrm{DM_{host}}/(1+z) + \mathrm{DM_{MW}} + \mathrm{DM_{MW,halo}} + \mathrm{DM_{IGM}}$, where $\mathrm{DM_{FRB}} = 103.5 \pm 0.3$ pc cm^{-3}. Table 8 summarizes the individual DM components and their respective priors. Similar to Keane et al. (2016) and Williams & Berger (2016), we modeled the Milky Way disk DM ($\mathrm{DM_{MW}}$) as a Gaussian with a mean equal to the minimum of the two Galactic DM model predictions = 33 pc cm^{-3} (see Table 2; the maximum redshift estimate would be larger, and so more conservative), and a standard deviation (σ) = 20% of the mean $\mathrm{DM_{MW}}$ value, a commonly assumed uncertainty for both the models (Cordes & Lazio 2002; Yao et al. 2017). Moreover, this is in agreement with the maximum DM estimate of the Milky Way disk along the FRB sight line using the $\overline{\mathrm{DM}\sin|b|}$ estimate from Ocker et al. (2020) (see Section 2.1). For $\mathrm{DM_{MW,halo}}$, we assumed a Gaussian distribution such that at 3σ, the $\mathrm{DM_{MW,halo}}$ is either 0 or 80 pc cm^{-3}. This choice is motivated to account for the large uncertainty in the Milky Way halo DM contribution (Keating & Pen 2020).

For $\mathrm{DM_{host}}$, we assumed a log-normal probability distribution as suggested by Macquart et al. (2020),

$$p(\mathrm{DM_{host}}) = \frac{1}{\mathrm{DM_{host}}\sigma_{\mathrm{host}}\sqrt{2\pi}} \times \exp\left[-\frac{(\log(\mathrm{DM_{host}}) - \mu_{\mathrm{host}})^2}{2\sigma_{\mathrm{host}}^2}\right], \quad \text{(A1)}$$

with $e^{\mu_{\mathrm{host}}} = 68.2$ pc cm^{-3} and $\sigma_{\mathrm{host}} = 0.88$. Similarly, for $\mathrm{DM_{IGM}}$, we use a semi-analytical model that Macquart et al. (2020) computed to quantify the uncertainty in $\mathrm{DM_{IGM}}$ at a given redshift (z):

$$\mathrm{p_{IGM}}(\Delta) = A\Delta^{-\beta}\exp\left[\frac{-(\Delta^{-\alpha} - C_0)^2}{2\alpha^2\sigma_1^2}\right], \quad \text{(A2)}$$

where $\Delta = \mathrm{DM_{IGM}}/\overline{\mathrm{DM_{IGM}}(z)}$, C_0 is the normalization constant, $\sigma_1 = 0.2\ z^{-0.5}$, $\alpha = 3$, $\beta = 3$, and $\overline{\mathrm{DM_{IGM2}}(z)}$ is the average $\mathrm{DM_{IGM}}$ estimate which is a function of redshift and assumed cosmology,[27] defined in Equation (2) of Macquart et al. (2020).

For the MCMC sampling, we used the `emcee` package (Foreman-Mackey et al. 2013), which implements an affine-invariant sampling algorithm proposed by Goodman & Weare (2010). We use 256 walkers of 20,000 samples after discarding 1000 burn-in samples from each walker, and thinned the samples by a factor of 100. To assess the convergence of the samplings, we estimated the mean proposal acceptance fraction = 42%, and the chain autocorrelation length ≈1.43. Both of the estimates are within the acceptable range. Lastly, we also estimated convergence criterion for the redshift parameter, $\hat{R} \approx 1.09$ which implies good convergence of the MCMC (Gelman et al. 2013). Figure 6 shows the corner plot produced from the MCMC analysis.

Table 8
Parameters Used in the MCMC Analysis Described in Appendix A

Parameter	Symbol	Units	Prior
Host galaxy redshift	z	...	U(10^{-4}, 1)
Host galaxy DM	$\mathrm{DM_{host}}$	pc cm^{-3}	LN($e^{68.2}$, 0.88)
Milky Way DM	$\mathrm{DM_{MW}}$	pc cm^{-3}	N(33, 20% × 33)
Milky Way halo DM	$\mathrm{DM_{MW,halo}}$	pc cm^{-3}	N(40, 33.33% × 40)
IGM DM	$\mathrm{DM_{IGM}}$	pc cm^{-3}	Equation (4) from Macquart et al. (2020)

[27] We adopt the Planck cosmological parameters (Planck Collaboration et al. 2016).

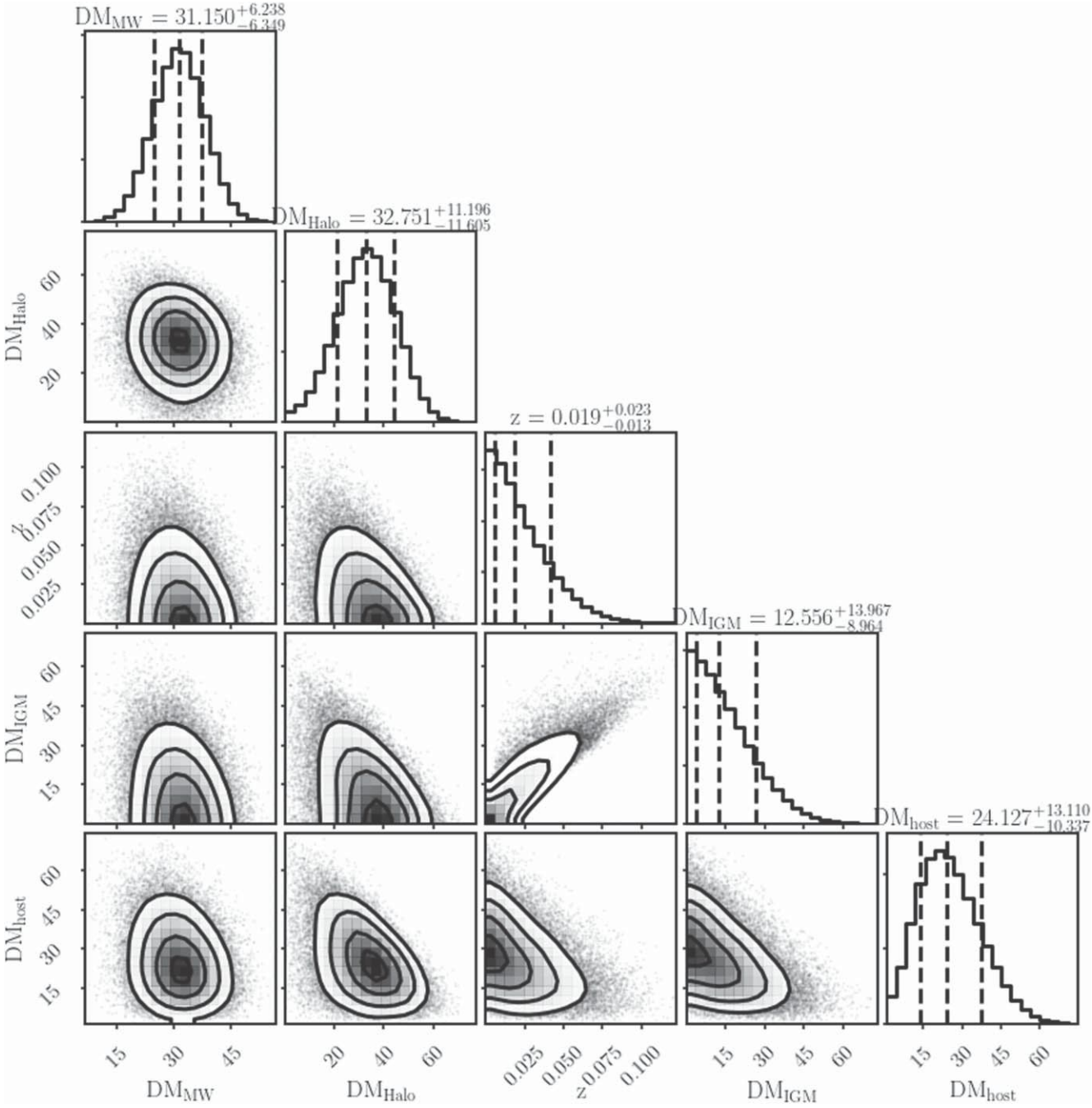

Figure 6. The results of a Markov-Chain Monte Carlo (MCMC) analysis discussed in Appendix A. Constraints on different FRB 20181030A DM components are derived using a Bayesian framework. The marginalized distribution for each DM component is shown along the diagonal of the corner plot. All DM units are in pc cm^{-3}.

From the MCMC analysis, we marginalized the redshift posterior over all other priors and calculated a one-sided 95% Bayesian credible upper limit = 0.05. This is the maximum redshift of FRB 20181030A used in our analysis.

Appendix B
Long-slit Spectroscopy of NGC 3252

We acquired the long-slit data of NGC 3252 in order to estimate the physical properties of NGC 3252, such as nebular metallicity and dust extinction. Here we discuss the steps for reducing the NGC 3252 long-slit spectroscopy data. In Figure 7, we show the zones used for the extraction of spectra along the long-slit. Hα and other nebular lines are traced over a zone of $\sim$90″ (8.7 kpc) which covers the entire bright optical extent of the galaxy. Several emission knots are seen along the slit, especially in the Hα spectral image. Each knot represents an H II region in the host galaxy. The presence of these H II regions allows us to obtain physical quantities along the slit using the physics of photoionized nebulae (Osterbrock & Ferland 2006). In order to maximize the S/N of the extracted spectra, we defined six zones, identified by letters a–f, in such a way that each zone contains at least one of the emission knots. The zone c spectrum contains the nucleus and the zone f

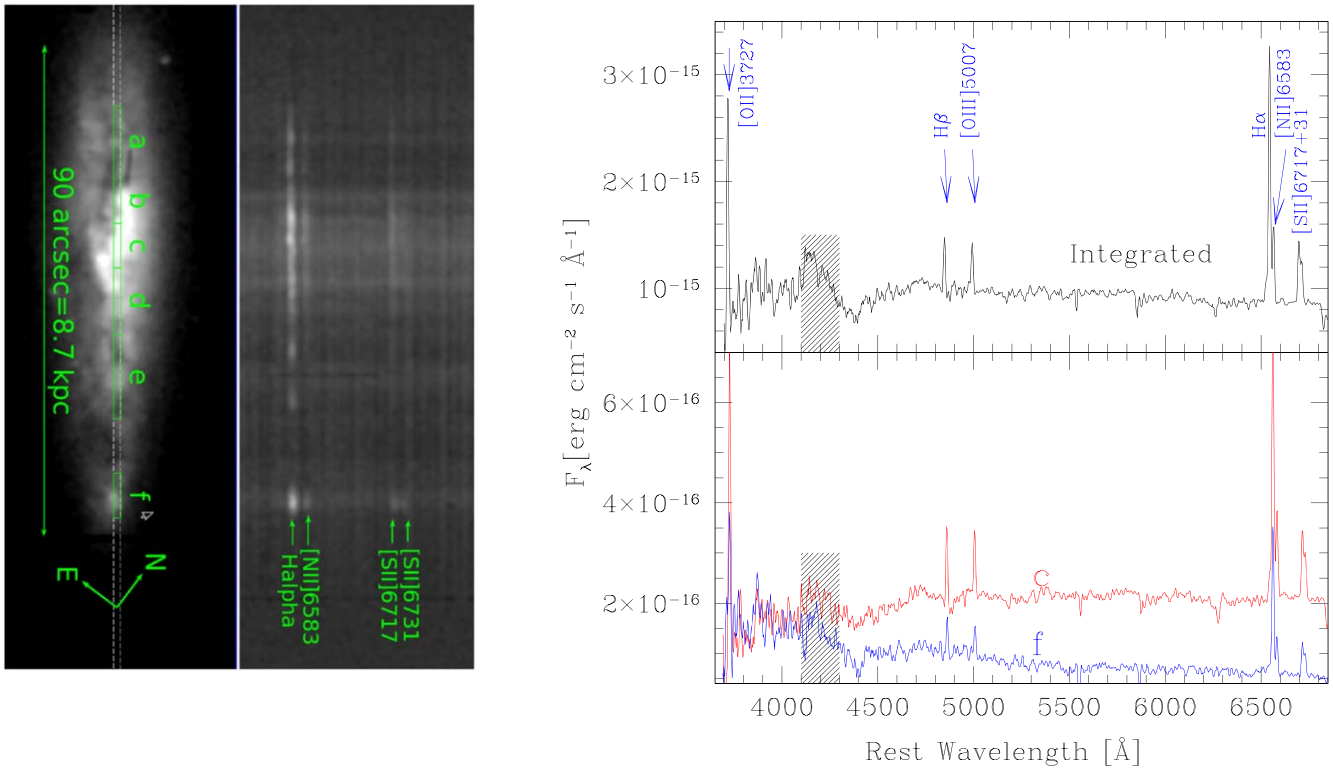

Figure 7. (Left) GTC/OSIRIS *r*-band acquisition image showing the position of the long slit (white dashed rectangle; PA = 37.°31) and the zones a–f selected for the spectral extraction (green rectangles). The image scale and orientation are shown. (Center) Spectral image along the long slit showing prominent emission lines in the red part of the spectrum. (Right) Rest-frame spectra, where the top spectrum was obtained by summing the rest-frame spectra of all the six zones denoted a–f. Spectra marked "c" and "f" correspond to the zone passing through the nucleus and a bright H II, respectively. Note that the latter region lies almost at the center of the 90% localization ellipse of the FRB source shown (see Figure 2). A bump in the spectra between 4100 and 4300 Å is due to a detector artifact, which is shown by shaded box.

Table 9
Physical Quantities from Long-slit Spectra of NGC 3252

Quantity[a]	a	b	c	d	e	f	Integrated
R.A.(J2000)	10:34:25.50	10:34:23.94	10:34:22.73	10:34:21.27	10:34:19.26	10:34:16.11	
Decl.(J2000)	+73:46:05.0	+73:45:56.4	+73:45:49.7	+73:45:41.6	+73:45:30.5	+73:45:13.1	
Area[″ × ″]	13.3 × 1.2	8.2 × 1.2	8.2 × 1.2	12.3 × 1.2	15.3 × 1.2	8.2 × 1.2	65.5 × 1.2
I([O II]3727)	38.5 ± 4.6	556.7 ± 3.7	498.2 ± 11.1	769.8 ± 9.5	412.4 ± 8.2	168.7 ± 0.3	437.0 ± 4.5
I(Hβ)	100.0	100.0	100.0	100.0	100.0	100.0	100.0
I([O III]5007)	79.8 ± 0.1	51.7 ± 4.0	84.2 ± 2.8	89.3 ± 1.3	51.4 ± 5.6	74.0 ± 0.5	77.4 ± 1.0
I(Hα)	287.0 ± 53.1	287.0 ± 66.3	287.0 ± 29.8	287.0 ± 38.8	287.0 ± 75.0	287.0 ± 37.4	287.0 ± 32.2
I([N II]6583)	96.1 ± 14.1	82.7 ± 16.1	89.9 ± 7.6	87.7 ± 9.3	69.0 ± 8.2	61.9 ± 4.1	80.6 ± 7.0
I([S II]6717)	53.8 ± 5.9	61.7 ± 9.5	62.2 ± 4.1	67.8 ± 6.7	58.2 ± 2.9	63.5 ± 3.0	60.6 ± 3.7
I([S II]6731)	25.1 ± 0.1	42.5 ± 4.6	47.4 ± 2.1	45.9 ± 3.2	44.9 ± 1.2	41.6 ± 0.1	45.0 ± 0.3
log F(Hβ_0)[erg cm^{-2} s^{-1}]	−14.50 ± 0.20	−14.25 ± 0.19	−14.25 ± 0.11	−14.02 ± 0.14	−14.28 ± 0.29	−14.62 ± 0.16	−13.50 ± 0.11
A_V[mag]	0.9 ± 0.4	1.4 ± 0.4	0.9 ± 0.2	1.6 ± 0.2	1.6 ± 0.4	0.8 ± 0.3	1.3 ± 0.2
EW(Hβ)[Å]	12.4	11.1	7.3	3.3	2.9	8.6	5.8
Velocity [km s^{-1}]	1073 ± 43	1105 ± 49	1056 ± 35	1125 ± 15	1166 ± 57	1274 ± 50	1133 ± 79
12+log(O/H)	8.64 ± 0.05	8.38 ± 0.05	8.46 ± 0.05	8.38 ± 0.05	8.37 ± 0.05	8.49 ± 0.05	8.44 ± 0.05

Note.
[a] In the first block, center coordinates of the rectangular zones (named a to f; see Figure 3) chosen for the extraction of spectra are given. The next block contains the extinction-corrected fluxes of prominent nebular lines relative to the flux of the Hβ line, i.e., $I(\lambda) = 100 \times F(\lambda)/F(\mathrm{H}\beta)$. The last block contains the extinction-corrected Hβ flux and physical quantities derived from the diagnostics of the nebular lines.

spectrum corresponds to a bright H II region to the southwest of the nucleus. This H II region lies almost at the center of the 90% localization ellipse of the FRB source shown in Figure 2. In the right panel, we show the extracted spectrum for these two regions. Each extracted spectrum was analyzed to measure the fluxes of bright nebular lines using the Gaussian fitting technique of the *splot* task in IRAF, which also performs a measurement and subtraction of continuum flux. The prominent lines in the spectrum were identified and are shown in the top panel. A deblending algorithm was used to extract accurate

fluxes of [N II]λ6548 and [N II]λ6583 lines in the presence of the bright Hα line and also to resolve the [S II] doublet.

The measured line fluxes in each spectrum are given in Table 9. The spectra were first corrected for Doppler shift using a mean of the recessional velocities measured using the Hβ, Hα, and [O III]λ5007 lines in each spectrum. The measured velocities are also given in Table 9. All six rest-frame spectra were summed to get an integrated spectrum of the galaxy, which is shown in the top right panel in Figure 7. Values measured for the integrated spectrum are given in the last column of Table 9. The mean of the velocities of the six extracted spectra was taken as the velocity of the integrated spectrum, which agrees very well with the systemic velocity of $1156 \pm 6\,\mathrm{km\,s^{-1}}$ reported in NED (Schneider et al. 1992). The Hα and Hβ emission line fluxes stated in Table 9 are used to obtain the visual extinction A_V experienced in each zone, shown in Figure 7, following the Balmer decrement method for case B recombination of a typical photoionized nebula ($T_e = 10{,}000$ K, $n_e = 100$ cm^{-3}; Osterbrock & Ferland 2006) and the reddening curve of Cardelli et al. (1989). We corrected the observed Hα and Hβ fluxes for the effects of the underlying stellar absorption by assuming an absorption equivalent width of 2 Å following McCall et al. (1985). The resulting A_V values vary between 0.8 and 1.6 mag in the zones along the slit. The line fluxes were corrected for the measured extinction and are given as ratios with respect to the flux of the Hβ line, which is multiplied by 100 following the normal convention.

Electron temperature-sensitive auroral lines were not detected in any of the extracted spectra. However, nebular lines for the determination of the oxygen and nitrogen abundances using the strong-line method are detected with $S/N > 10$. We used the calibrations of Pilyugin & Grebel (2016) for this purpose (their Equations (4) and (13)). The resulting values of 12+log(O/H) are given in Table 9 for each zone as well as that measured in the integrated spectrum.

Appendix C
Stellar Population Synthesis Using `Prospector`

We infer several physical properties of NGC 3252 (at 20 Mpc) using a python-based Bayesian inference code, `Prospector` (Leja et al. 2017; Johnson et al. 2019), which estimates galaxy properties using stellar population synthesis models defined within the framework of the Flexible Stellar Populations Synthesis (FSPS) stellar populations code (Conroy et al. 2009). `Prospector` provides an MCMC framework via `emcee` to fit observed SEDs and estimate posterior distribution for each free parameters. In this paper, we use `Prospector` to estimate the stellar mass, metallicity, and mass-weighted stellar population age of NGC 3252. We use 17 broadband filters from the GALEX FUV filter at 1549 Å through the Herschel telescope bands that provide coverage at FIR wavelengths as shown in Figure 4 and Table 10.

All flux densities are estimated after correcting for the Milky Way extinction. We fit a delayed τ star formation history model (Simha et al. 2014; Carnall et al. 2019) with five free parameters: metallicity, mass-weighted stellar population age, star formation timescale, and V-band optical extinction (=1.086 × dust2), which are described in Table 11. In this model, the star formation history is proportional to $t \times \exp(-t/\tau)$, where t is the time since the formation epoch of the galaxy, and τ is the characteristic decay time of our star formation history. Additionally, we enabled nebular emission (Byler et al. 2017) and dust emission (Draine & Li 2007) models in the FSPS framework along with a standard dust-attenuation model from Calzetti et al. (2000). Finally, all five parameters are given standard `Prospector` priors, except $\log(Z/Z_\odot)$, which is informed by the constraints derived in Section 2.4. This is included to reduce the effect of the age–metallicity degeneracy (Worthey 1994). We used a Gaussian prior to model $\log(Z/Z_\odot)$ with mean = − 0.25 derived in Section 2.4 using optical spectral lines. However, we increased the σ value by a factor of three to account for any potential bias in converting the oxygen abundance to nebular metallicity, a conservative choice given that the conversion error is typically ∼0.02 (Serenelli et al. 2009), which is less than one sigma error on the $\log(Z_{gas}/Z_\odot)$, i.e., 0.07 (see Table 6).

Using this framework, we derived a metallicity fraction, $\log(Z/Z_\odot) = -0.21^{+0.18}_{-0.19}$, and the present-day stellar mass of the galaxy $= 5.8^{+1.6}_{-2.0} \times 10^9 M_\odot$. To estimate the best-fitted

Table 10
17 Broadband Filters Used to Model the SED of NGC 3252

Instrument[a]	Filter	Effective Wavelength Å	Flux Density[b,c] maggies
GALEX	FUV	1549	4.38×10^{-7}
	NUV	2304	5.56×10^{-7}
DESI[d]	*g*	4670	4.98×10^{-6}
	r	6156	9.26×10^{-6}
	z	8917	1.41×10^{-5}
2MASS	*J*	12319	1.75×10^{-5}
	H	16420	1.79×10^{-5}
	Ks	21567	1.67×10^{-5}
WISE	W1	33461	9.75×10^{-6}
	W2	45952	6.33×10^{-6}
	W3	115526	1.99×10^{-5}
	W4	220783	2.50×10^{-5}
Herschel	PACS(Green)	979036	8.40×10^{-4}
	PACS(RED)	1539451	1.13×10^{-3}
	SPIRE(PSW)	2428393	5.87×10^{-4}
	SPIRE(PMW)	3408992	3.00×10^{-4}
	SPIRE(PLW)	4822635	1.27×10^{-4}

Notes.
[a] Except for the DESI survey, all instruments' flux densities are obtained from the aperture-matched photometry catalog of nearby galaxies by Clark et al. (2018).
[b] Note that 1 maggie is defined as the flux density in Janskys divided by 3631. Fluxes at $\lambda < 100000$ Å are corrected for Galactic extinction according to the prescription of Schlafly & Finkbeiner (2011).
[c] All broadband fluxes are assigned a 20% fractional uncertainty.
[d] For DESI filter magnitudes, we used the photometric redshift catalog by Zhou et al. (2020).

Table 11
Free Parameters and Their Associated Priors for the `Prospector` "Delayed-τ" Model

Parameter	Description	Prior
$\log(M/M_{\odot})$	total stellar mass formed	uniform: min = 8, max = 11
$\log(Z/Z_{\odot})$	stellar metallicity	Gaussian: mean = −0.25, $\sigma = 0.21$
dust2	diffuse V-band dust optical depth	top-hat: min = 0.0, max = 3.0
$t_{\rm age}$ [Gyr]	stellar population age of NGC 3252	top-hat: min = 0.01, max = 13.6
τ [Gyr]	e-folding time of the SFH	uniform: min = 0.1, max = 30

mass-weighted stellar population age value, we used Equation (5) of Carnall et al. (2019) and found it to be $4.8^{+1.6}_{-1.8}$ Gyr. All these values are provided in Table 6. Note that the quoted uncertainties in all cases are 1σ values.

ORCID iDs

M. Bhardwaj https://orcid.org/0000-0002-3615-3514
A. Yu. Kirichenko https://orcid.org/0000-0002-8139-8414
D. Michilli https://orcid.org/0000-0002-2551-7554
Y. D. Mayya https://orcid.org/0000-0002-4677-0516
V. M. Kaspi https://orcid.org/0000-0001-9345-0307
B. M. Gaensler https://orcid.org/0000-0002-3382-9558
M. Rahman https://orcid.org/0000-0003-1842-6096
S. P. Tendulkar https://orcid.org/0000-0003-2548-2926
E. Fonseca https://orcid.org/0000-0001-8384-5049
Alexander Josephy https://orcid.org/0000-0003-3059-6223
C. Leung https://orcid.org/0000-0002-4209-7408
Marcus Merryfield https://orcid.org/0000-0003-2095-0380
Emily Petroff https://orcid.org/0000-0002-9822-8008
Z. Pleunis https://orcid.org/0000-0002-4795-697X
Pranav Sanghavi https://orcid.org/0000-0001-5504-229X
P. Scholz https://orcid.org/0000-0002-7374-7119
K. Shin https://orcid.org/0000-0002-6823-2073
Kendrick M. Smith https://orcid.org/0000-0002-2088-3125
I. H. Stairs https://orcid.org/0000-0001-9784-8670

References

Arora, N., Stone, C., Courteau, S., & Jarrett, T. H. 2021, MNRAS, 505, 3135
Asplund, M., Grevesse, N., Sauval, A. J., & Scott, P. 2009, ARA&A, 47, 481
Astropy Collaboration, Price-Whelan, A. M., Sipőcz, B. M., et al. 2018, AJ, 156, 123
Astropy Collaboration, Robitaille, T. P., Tollerud, E. J., et al. 2013, A&A, 558, A33
Bade, N., Engels, D., Voges, W., et al. 1998, A&AS, 127, 145
Bailes, M., Bassa, C. G., Bernardi, G., et al. 2021, MNRAS, 503, 5367
Bauer, F. E., Condon, J. J., Thuan, T. X., & Broderick, J. J. 2000, ApJS, 129, 547
Bhardwaj, M., Gaensler, B. M., Kaspi, V. M., et al. 2021, ApJL, 910, L18
Bochenek, C. D., Ravi, V., Belov, K. V., et al. 2020, Natur, 587, 7832
Bohlin, R. C., Colina, L., & Finley, D. S. 1995, AJ, 110, 1316
Buat, V., Takeuchi, T. T., Iglesias-Páramo, J., et al. 2007, ApJS, 173, 404
Burke-Spolaor, S. 2018, NatAs, 2, 845
Byler, N., Dalcanton, J. J., Conroy, C., & Johnson, B. D. 2017, ApJ, 840, 44
Calzetti, D., Armus, L., Bohlin, R. C., et al. 2000, ApJ, 533, 682
Cardelli, J. A., Clayton, G. C., & Mathis, J. S. 1989, ApJ, 345, 245
Carnall, A. C., Leja, J., Johnson, B. D., et al. 2019, ApJ, 873, 44
Chatterjee, S., Law, C., Wharton, R., et al. 2017, Natur, 541, 58
Chatterjee, S., Vlemmings, W., Brisken, W., et al. 2005, ApJL, 630, L61
Chen, G., Ravi, V., & Lu, W. 2020, ApJ, 897, 146
CHIME/FRB Collaboration 2021, ATel, 14497
CHIME/FRB Collaboration, Amiri, M., Andersen, B. C., et al. 2020a, Natur, 582, 351
CHIME/FRB Collaboration, Amiri, M., Bandura, K., et al. 2018, ApJ, 863, 48
CHIME/FRB Collaboration, Andersen, B. C., Bandura, K., et al. 2019, ApJL, 885, L24
CHIME/FRB Collaboration, Andersen, B. C., Bandura, K. M., et al. 2020b, Natur, 587, 54
Clark, C. J. R., Verstocken, S., Bianchi, S., et al. 2018, A&A, 609, A37
Condon, J. J., Cotton, W., Greisen, E., et al. 1998, AJ, 115, 1693
Condon, J. J., Yin, Q. F., Thuan, T. X., & Boller, T. 1998, AJ, 116, 2682
Conroy, C., Gunn, J. E., & White, M. 2009, ApJ, 699, 486
Cordes, J. M., & Lazio, T. J. W. 2002, arXiv:astro-ph/0207156
Cruces, M., Spitler, L. G., Scholz, P., et al. 2020, MNRAS, 500, 448
Dale, D. A., & Helou, G. 2002, ApJ, 576, 159
Davies, L. J. M., Huynh, M. T., Hopkins, A. M., et al. 2017, MNRAS, 466, 2312
de Vaucouleurs, G., de Vaucouleurs, A., Corwin, H. G., Jr., et al. 1991, Third Reference Catalogue of Bright Galaxies (Berlin: Springer)
Dey, A., Schlegel, D. J., Lang, D., et al. 2019, AJ, 157, 168
Dolag, K., Gaensler, B. M., Beck, A. M., & Beck, M. C. 2015, MNRAS, 451, 4277
Draine, B. T., & Li, A. 2007, ApJ, 657, 810
Driver, S. P., Andrews, S. K., Davies, L. J., et al. 2016, ApJ, 827, 108
Fong, W.-f., Dong, Y., Leja, J., et al. 2021, arXiv:2106.11993
Fonseca, E., Andersen, B. C., Bhardwaj, M., et al. 2020, ApJL, 891, L6
Foreman-Mackey, D., Hogg, D. W., Lang, D., & Goodman, J. 2013, PASP, 125, 306
Fruchter, A. S., Levan, A. J., Strolger, L., et al. 2006, Natur, 441, 463
Fukugita, M., Hogan, C., & Peebles, P. 1998, ApJ, 503, 518
Fullmer, L., & Londsale, C. J. 1989, JPL D-1932, 3
Gelman, A., Carlin, J. B., Stern, H. S., et al. 2013, Bayesian Data Analysis (Boca Raton, FL: CRC Press)
Goldstein, A., Cleveland, W. H., & Kocevski, D. 2021, GBM Data Tools: v1.1.0, https://fermi.gsfc.nasa.gov/ssc/data/analysis/gbmFermi
Gómez-González, V. M. A., Mayya, Y. D., & Rosa-González, D. 2016, MNRAS, 460, 1555
Gómez-Velarde, G., García-Alvarez, D., & Cabrerra-Lavers, A. 2016, in ASP Conf. Ser. 507, Multi-Object Spectroscopy in the Next Decade: Big Questions, Large Surveys, and Wide Fields, ed. I. Skillen, M. Balcells, & S. Trager (San Francisco, CA: ASP), 191
González-Serrano, J. I., Sánchez-Portal, M., Castañeda, H., et al. 2004, ExA, 18, 65
Goodman, J., & Weare, J. 2010, Commun. Appl. Math. Comput. Sci., 5, 65
Gourdji, K., Michilli, D., Spitler, L. G., et al. 2019, ApJL, 877, L19
Greco, J. P., Greene, J. E., Strauss, M. A., et al. 2018, ApJ, 857, 104
Haakonsen, C. B., & Rutledge, R. E. 2009, ApJS, 184, 138
Hafen, Z., Faucher-Giguère, C.-A., Anglés-Alcázar, D., et al. 2019, MNRAS, 488, 1248
Hancock, P. J., Murphy, T., Gaensler, B. M., Hopkins, A., & Curran, J. R. 2012, MNRAS, 422, 1812
Hancock, P. J., Trott, C. M., & Hurley-Walker, N. 2018, PASA, 35, e011
Harris, C. R., Millman, K. J., van der Walt, S. J., et al. 2020, Natur, 585, 357
Heintz, K. E., Prochaska, J. X., Simha, S., et al. 2020, ApJ, 903, 152
Hinton, S. R., Davis, T. M., Lidman, C., Glazebrook, K., & Lewis, G. F. 2016, A&C, 15, 61
Huchra, J., Davis, M., Latham, D., & Tonry, J. 1983, ApJS, 52, 89
Hunter, J. D. 2007, CSE, 9, 90
Iglesias-Páramo, J., Buat, V., Donas, J., Boselli, A., & Milliard, B. 2004, A&A, 419, 109
Iglesias-Páramo, J., Buat, V., Takeuchi, T. T., et al. 2006, ApJS, 164, 38
Intema, H., Jagannathan, P., Mooley, K., & Frail, D. 2017, A&A, 598, A78
Johnson, B. D., Leja, J. L., Conroy, C., & Speagle, J. S. 2019, Prospector: Stellar population inference from spectra and SEDs, Astrophysics Source Code Library, ascl:1905.025
Joye, W. A., & Mandel, E. 2003, in ASP Conf. Ser. 295, Astronomical Data Analysis Software and Systems XII, ed. H. E. Payne, R. I. Jedrzejewski, & R. N. Hook (San Francisco, CA: ASP), 489
Kaaret, P., Koutroumpa, D., Kuntz, K. D., et al. 2020, NatAs, 4, 1072

Kasliwal, M. 2011, in The Gravitational-wave Physics and Astronomy Workshop, 2011 January 26–29, http://www.gravity.phys.uwm.edu/conferences/gwpaw/program/talks.html
Keane, E. F., Johnston, S., Bhandari, S., et al. 2016, Natur, 530, 453
Keating, L. C., & Pen, U.-L. 2020, MNRAS, 496, L106
Kennicutt, R. C., Jr., Tamblyn, P., & Congdon, C. E. 1994, ApJ, 435, 22
Kirsten, F., Marcote, B., Nimmo, K., et al. 2021, arXiv:2105.11445
Klein, U., Lisenfeld, U., & Verley, S. 2018, A&A, 611, A55
Klypin, A., Yepes, G., Gottlöber, S., Prada, F., & Heß, S. 2016, MNRAS, 457, 4340
Kourkchi, E., & Tully, R. B. 2017, ApJ, 843, 16
Kwiatkowski, D. 2015, arXiv:1512.00678
Lacy, M., Baum, S. A., Chandler, C. J., et al. 2016, AAS, 227, 324
Leitherer, C. 2005, in AIP Conf. Ser. 761, The Spectral Energy Distributions of Gas-Rich Galaxies: Confronting Models with Data, ed. C. C. Popescu & R. J. Tuffs (Melville, NY: AIP), 39
Leja, J., Johnson, B. D., Conroy, C., van Dokkum, P. G., & Byler, N. 2017, ApJ, 837, 170
Li, C., Lin, L., Xiong, S., et al. 2021, NatAs, 5, 378
Li, Y., & Zhang, B. 2020, ApJL, 899, L6
Li, Y., Zhang, B., Nagamine, K., & Shi, J. 2019, ApJL, 884, L26
Lim, S. H., Mo, H. J., Lu, Y., Wang, H., & Yang, X. 2017, MNRAS, 470, 2982
Lorimer, D. R., Bailes, M., McLaughlin, M. A., Narkevic, D. J., & Crawford, F. 2007, Sci, 318, 777
Lu, W., & Kumar, P. 2016, MNRAS, 461, L122
Lu, W., & Piro, A. L. 2019, ApJ, 883, 40
Luo, R., Men, Y., Lee, K., et al. 2020, MNRAS, 494, 665
Lyubarsky, Y. 2021, Univ, 7, 56
Macquart, J.-P., Prochaska, J., McQuinn, M., et al. 2020, Natur, 581, 391
Maller, A. H., & Bullock, J. S. 2004, MNRAS, 355, 694
Mannings, A. G., Fong, W.-f., Simha, S., et al. 2021, ApJ, 917, 75
Maoz, D. 2007, MNRAS, 377, 1696
Marvil, J., Owen, F., & Eilek, J. 2015, AJ, 149, 32
Masters, K. L., Crook, A., Hong, T., et al. 2014, MNRAS, 443, 1044
McCall, M. L., Rybski, P. M., & Shields, G. A. 1985, ApJS, 57, 1
McMullin, J. P., Waters, B., Schiebel, D., Young, W., & Golap, K. 2007, in ASP Conf. Ser. 376, Astronomical Data Analysis Software and Systems XVI, ed. R. A. Shaw, F. Hill, & D. J. Bell (San Francisco, CA: ASP), 127
Mereghetti, S., Savchenko, V., Ferrigno, C., et al. 2020, ApJL, 898, L29
Metzger, B. D., Berger, E., & Margalit, B. 2017, ApJ, 841, 14
Metzger, B. D., Margalit, B., & Sironi, L. 2019, MNRAS, 485, 4091
Michilli, D., Masui, K. W., Mckinven, R., et al. 2021, ApJ, 910, 147
Moster, B. P., Naab, T., & White, S. D. M. 2013, MNRAS, 428, 3121
Nicastro, L., Guidorzi, C., Palazzi, E., et al. 2021, Univ, 7, 76
Nicholl, M., Williams, P. K. G., Berger, E., et al. 2017, ApJ, 843, 84
Ocker, S. K., Cordes, J. M., & Chatterjee, S. 2020, ApJ, 897, 124
Oke, J. B. 1974, ApJS, 27, 21
Oke, J. B. 1990, AJ, 99, 1621
Osterbrock, D. E., & Ferland, G. J. 2006, Astrophysics of Gaseous Nebulae and Active Galactic Nuclei (Mill Valley, CA: Univ. Science Books)
Palmer, D. M., Barthelmy, S., Gehrels, N., et al. 2005, Natur, 434, 1107
Pilyugin, L. S., & Grebel, E. K. 2016, MNRAS, 457, 3678
Planck Collaboration, Ade, P. A. R., Aghanim, N., et al. 2016, A&A, 594, A13
Platts, E., Weltman, A., Walters, A., et al. 2019, Phys. Rep., 821, 1
Rajwade, K. M., Mickaliger, M. B., Stappers, B. W., et al. 2020, MNRAS, 495, 3551
Ravi, V., Law, C. J., Li, D., et al. 2021, arXiv:2106.09710
Rengelink, R., Tang, Y., De Bruyn, A., et al. 1997, A&AS, 124, 259
Resmi, L., Vink, J., & Ishwara-Chandra, C. H. 2020, arXiv:2010.14334
Ridnaia, A., Svinkin, D., Frederiks, D., et al. 2021, NatAs, 5, 372
Robitaille, T., & Bressert, E. 2012, APLpy: Astronomical Plotting Library in Python, Astrophysics Source Code Library, ascl:1208.017
Salo, H., Laurikainen, E., Laine, J., et al. 2015, ApJS, 219, 4
Schlafly, E. F., & Finkbeiner, D. P. 2011, ApJ, 737, 103
Schneider, S. E., Thuan, T. X., Mangum, J. G., & Miller, J. 1992, ApJS, 81, 5
Scholz, P., Cook, A., Cruces, M., et al. 2020, ApJ, 901, 165
Serenelli, A. M., Basu, S., Ferguson, J. W., & Asplund, M. 2009, ApJL, 705, L123
Simha, V., Weinberg, D. H., Conroy, C., et al. 2014, arXiv:1404.0402
Tanoglidis, D., Drlica-Wagner, A., Wei, K., et al. 2021, ApJS, 252, 18
Tauris, T. M., Sanyal, D., Yoon, S. C., & Langer, N. 2013, A&A, 558, A39
Taylor, M., Cinabro, D., Dilday, B., et al. 2014, ApJ, 792, 135
Tempel, E., Kipper, R., Tamm, A., et al. 2016, A&A, 588, A14
Tendulkar, S. P., Bassa, C., Cordes, J. M., et al. 2017, ApJL, 834, L7
The CHIME/FRB Collaboration, Amiri, M., Andersen, B. C., et al. 2021, arXiv:2106.04352
Thornton, D., Stappers, B., Bailes, M., et al. 2013, Sci, 341, 53
Tody, D. 1986, Proc. SPIE, 627, 733
Tody, D. 1993, in ASP Conf. Ser. 52, Astronomical Data Analysis Software and Systems II, ed. R. J. Hanisch, R. J. V. Brissenden, & J. Barnes (San Francisco, CA: ASP), 173
Truemper, J. 1982, AdSpR, 2, 241
Tully, R. B. 2015, AJ, 149, 171
Tully, R. B., Courtois, H. M., & Sorce, J. G. 2016, AJ, 152, 50
Tumlinson, J., Peeples, M. S., & Werk, J. K. 2017, ARA&A, 55, 389
Ueda, Y., Ishisaki, Y., Takahashi, T., Makishima, K., & Ohashi, T. 2001, ApJS, 133, 1
van den Bergh, S., Li, W., & Filippenko, A. V. 2005, PASP, 117, 773
von Kienlin, A., Meegan, C. A., Paciesas, W. S., et al. 2020, ApJ, 893, 46
Williams, P. K. G., & Berger, E. 2016, ApJL, 821, L22
Worthey, G. 1994, ApJS, 95, 107
Yamasaki, S., & Totani, T. 2020, ApJ, 888, 105
Yao, J., Manchester, R., & Wang, N. 2017, ApJ, 835, 29
Yaron, O., Ofek, E., Gal-Yam, A., & Sass, A. 2020, TNSAN, 70, 1
Yi, S.-X., Gao, H., & Zhang, B. 2014, ApJL, 792, L21
Zhou, P., Zhou, X., Chen, Y., et al. 2020, ApJ, 905, 99
Zou, H., Gao, J., Zhou, X., & Kong, X. 2019, ApJS, 242, 8